

A $H\alpha$ metric for identifying dormant black holes in X-ray transients

J. Casares^{1,2}, M.A.P. Torres^{1,2} and S. Navarro Umpiérrez^{1,2}

¹ Instituto de Astrofísica de Canarias, E-38205 La Laguna, Tenerife, Spain

² Departamento de Astrofísica, Universidad de La Laguna, E-38206 La Laguna, Tenerife, Spain
e-mail: jorge.casares@iac.es

Received 27 January 2025; accepted 3 June 2025

ABSTRACT

Dormant black holes in X-ray transients can be identified by the presence of broad $H\alpha$ emission lines from quiescent accretion discs. Unfortunately, short-period cataclysmic variables can also produce broad $H\alpha$ lines, especially when viewed at high inclinations, and are thus a major source of contamination. Here we compare the full width at half maximum (FWHM) and equivalent width (EW) of the $H\alpha$ line in a sample of 20 quiescent black hole transients and 354 cataclysmic variables (305 from SDSS I to IV) with secure orbital periods (P_{orb}) and find that: (1) FWHM and EW values decrease with P_{orb} , and (2) for a given P_{orb} both parameters are typically larger in black hole transients than in cataclysmic variables. We also compile spectral types for 17 low-mass companions in black hole transients from the literature and derive an empirical $P_{\text{orb}} - T_{\text{eff}}$ calibration. Using this, we conclude that the decrease in EW with P_{orb} is mostly driven by the dilution of the $H\alpha$ flux by the donor star continuum, which dominates the r-band spectrum for $P_{\text{orb}} \gtrsim 0.2$ d. At shorter periods, the larger contribution of the disc to the total r-band flux introduces significant scatter in the EWs due to the changing visibility of the disc projected area with binary inclination. On the other hand, the larger EWs observed in black holes can be explained by their extreme mass ratios (which limit the fractional contribution of the companion to the total flux) and the absence of a white dwarf component (important at $P_{\text{orb}} \lesssim 0.085$ d). Finally, we present a tentative metric, based on $H\alpha$ FWHM and EW information, and provide optimal cuts to select $\sim 80\%$ of the black hole X-ray transients, while rejecting $\sim 78\%$ of the cataclysmic variables in our sample. Such a metric, combined with other multi-frequency diagnostics, can help detect new dormant black hole X-ray transients in blind large-scale surveys such as $H\alpha$ WKS and its pathfinder, Mini- $H\alpha$ WKS.

Key words. Accretion, accretion disks – Line: profiles – X-rays: binaries – Black hole physics – Stars: dwarf novae

1. Introduction

Over the past 50 years, black hole X-ray transients (BH XRTs) have provided us with special windows through which to study accretion processes in extreme environments, supernova explosions, and the evolution of close binary systems. In recent years, other BH populations have also been revealed by gravitational wave detectors (Abbott et al. 2019) and Gaia astrometry (e.g. Gaia Collaboration et al. 2024). In this context, XRTs remain a key benchmark for BH properties, as they are supposed to descend from a well-defined binary evolution channel at near solar metallicity, involving a common envelope phase (but see Naoz et al. 2016, also Burdge et al. 2024, for an alternative formation pathway in hierarchical triples).

With only 20 dynamically confirmed cases and another ≈ 50 candidates (Corral-Santana et al. 2016), the current sample of BH XRTs is severely limited by small numbers. In addition, the sample is X-ray selected, and thus biased towards transients with short recurrence times and high outburst luminosities (Wu et al. 2010; Lin et al. 2019). Other complex X-ray selection biases may also be at play, such as high-inclination BHs concealed by disc obscuration (Narayan & McClintock 2005; Corral-Santana et al. 2013), a potential lack of short-period (<4 h), radiatively inefficient BH transients (Kneivitt et al. 2014, see also Arur & Maccarone 2018), period gap BH XRTs with very low X-ray luminosities (Maccarone & Patruno 2013), or the possible existence of faint, persistent (i.e. non-transient) BH X-ray binaries with long orbital periods (Menou et al. 1999). In addition, both the Galactic distribution of XRTs and their BH masses are likely

to be shaped by natal kicks (Gandhi et al. 2020) and obscuration by interstellar extinction (Jonker et al. 2021). Similarly, while the existence of the so-called lower mass-gap (i.e. dearth of BHs with masses between $\approx 2 - 5 M_{\odot}$), appears robust against transient selection effects (Siegel et al. 2023), it depends critically on our ability to measure accurate masses in the presence of accretion disc contamination (Kreidberg et al. 2012). A significant step forward in the statistics of BH XRTs, with a more cleanly selected sample, is therefore fundamental to disentangling selection biases and advancing our knowledge of this reference population.

In an attempt to increase the number of BH XRTs, we have developed a series of scaling relations between fundamental binary parameters and the properties of the $H\alpha$ emission line, formed in the accretion disc around the BH (Casares 2015, 2016; Casares et al. 2022). In particular, a correlation between the $H\alpha$ full width at half maximum (FWHM) and the radial velocity semi-amplitude of the companion star (K_2) allows for the extraction of compact object mass functions in systems where the spectrum of the donor star is not detected (Casares 2015; hereafter C15). This requires independent knowledge of the orbital period, which can be obtained from light curve variability. If the FWHM is also measured photometrically, this opens up the new concept of ‘photometric mass function’, whereby BHs can be searched for and weighed photometrically in large fields of view, i.e. much more efficiently than by classical spectroscopy (see C15).

In Casares (2018) (hereafter C18), we present a proof of concept of how to obtain $H\alpha$ FWHMs using three custom inter-

ference filters of different widths. We also propose a new strategy (H α WKS, an acronym for ‘H α -Width Kilodegree survey’) optimised for the detection of dormant¹ BH XRTs in a blind survey of the Galactic plane. In addition to H α widths, the H α WKS photometric system also provides equivalent width (EW) information. Furthermore, as the three filters are centred at 6563 Å, the results are invariant to interstellar extinction and the spectral energy distribution of the objects. H α WKS was subsequently validated in a feasibility test, demonstrating that H α FWHM and EW values can be recovered within 10% accuracy in a sample of quiescent BH XRTs down to at least $r=22$ (Casares & Torres 2018). Essentially, H α WKS exploits the width of the Doppler-broadened H α line as a proxy for the deep gravitational fields of compact stars, enabling the efficient selection of dormant BHs. To some extent, the approach is similar to reverberation mapping techniques, whereby line widths from the broad line region are used to weigh super-massive BHs in active galactic nuclei (e.g. Peterson et al. 2004).

A search for dormant BHs with H α WKS would in principle be free from X-ray selection bias, although the strategy does favour the detection of accreting binaries with short periods and high inclinations (i.e. large H α widths). The main source of contamination at large FWHMs is expected to come from cataclysmic variables (CVs i.e. interacting binaries with accreting white dwarfs), which are extremely abundant compared to BH XRTs. Monte Carlo simulations have shown that a cut-off at $\text{FWHM} \geq 2200 \text{ km s}^{-1}$ removes $\approx 99.9\%$ of all the CVs, while retaining $\approx 50\%$ of the BHs (C18). The recovery of BHs with $\text{FWHM} < 2200 \text{ km s}^{-1}$ is quite challenging as the level of CV contamination increases dramatically. The aim of this paper is to develop a metric based on H α FWHMs and EW information from a large sample of quiescent BH XRTs and CVs, to help separate these two populations. The new diagnostic will provide an additional tool to identify dormant BH XRTs in single epoch spectra and special photometric H α surveys such as H α WKS and its pathfinder, Mini-H α WKS.

2. Updated collection of H α FWHM and EWs in quiescent BH XRTs

Table 1 gives a list of FWHM and EW measurements of the H α line in 20 quiescent BH XRTs. These were obtained from a spectroscopic database collected over several epochs spanning 30 years. The errors reported include systematic uncertainties to account for orbital and secular (inter-epoch) variability. Appendix A gives full details of the database (broken down into different epochs), how FWHM and EW values were measured, and the systematic uncertainties applied. The numbers for XTE J1650-500 should be treated with caution, as the only available spectra were taken just ≈ 9 months after the peak of the outburst, when the binary was still fading into quiescence (see Sánchez-Fernández et al. 2002, also Appendix A for a photometric verification). Similarly, the GX 339-4 off-state data from Heida et al. (2017) used here might not correspond to complete quiescence due to the frequent outburst activity characteristic of this system. It should be emphasised that the quiescent FWHM and EW values for each system are quite stable over time, despite orbital and secular variability (Appendix A).

¹We consider dormant BHs to be quiescent BH XRTs that will eventually trigger an outburst episode. Therefore, we will hereafter use the terms, ‘dormant’ and ‘quiescent’ interchangeably.

2.1. FWHM versus orbital period

Figure 1 displays the behaviour of the FWHM as a function of the orbital period (P_{orb}) for the ensemble of BH XRTs. For comparison, we also plot FWHM values of 43 quiescent CVs (mostly dwarf novae) from C15, using red triangles. This sample was selected from Ritter & Kolb’s catalogue (Ritter & Kolb 2003) based on accurate reports of the radial velocity curve of the companion star and is therefore prone to selection biases. In particular, it over-represents CVs with long P_{orb} , where the companion’s spectrum dominates, and eclipsing short P_{orb} CVs, where K_2 is inferred through light curve modelling. To compensate for the uneven P_{orb} distribution we have added 305 CVs from the Sloan Digital Sky Survey (SDSS) I to IV with secure P_{orb} determinations (Inight et al. 2023). The latter is a magnitude-limited spectroscopic sample and is therefore more uniformly selected. The SDSS CVs have been divided into three classes: magnetic (intermediate polars, polars, and pre-polars), novae-like, and dwarf novae (including WZ Sge, SU UMa, U Gem, and Z Cam sub-types). Eclipsing CVs are indicated by open triangles, although the list is likely to be incomplete as some SDSS CVs lack sufficient photometric coverage for eclipse detection. Typical FWHM uncertainties for SDSS CVs are smaller than the symbol size because they are obtained from individual (single epoch) spectra. More realistic uncertainties (including orbital and secular variability) have been estimated at the $\approx 7\%$ level in C15.

Figure 1 is an update of Fig. 9 from C18, with the addition of six more BH XRTs and the 305 SDSS CVs. Since FWHM scales with K_2 (C15), the mass function equation $P_{\text{orb}} K_2^3 / (2\pi G) = M_1 \sin^3 i / (1 + q)^2$ can be used to draw $P_{\text{orb}} - \text{FWHM}$ lines for a given set of compact object mass (M_1), mass ratio (q), and binary inclination (i). As a guide, we have marked an approximate upper bound for FWHM in CVs, based on the Chandrasekhar mass limit and a maximum binary inclination of $i = 90^\circ$. Here, we have also adopted the $P_{\text{orb}} - q$ relation $q = 0.73 - 11.55 \times \exp[-(P_{\text{orb}} + 0.39)/0.15]$, derived in C18, and the q dependence of the FWHM – K_2 correlation (equations 5 and 6 in C15). In addition, following C18 we have drawn a lower limit on FWHM for accretion disc eclipses of a representative $0.82 M_\odot$ white dwarf (Zorotovic et al. 2011). An upper limit on FWHM for the case of an extreme neutron star mass, $M_1 = 2.3 M_\odot$ (Ruiz et al. 2018; Shibata et al. 2019) at $i = 90^\circ$, is also indicated.

Figure 1 shows that, for a given P_{orb} , BH XRTs naturally produce broader H α lines than CVs due to the more massive central objects. As a matter of fact, BH XRTs closely follow the predicted FWHM – P_{orb} curve for a canonical BH mass of $M_1 = 7.8 M_\odot$ (Özel et al. 2010; Kreidberg et al. 2012) with a typical $q = 0.06$ (Casares 2016) and most probable inclination of $i = 60^\circ$ (dashed line). Only GRO J0422+32 and GX339-4 fall under the $2.3 M_\odot$ neutron star limit, placing them in the CV region. In the case of GRO J0422+32, this is consistent with a low-mass BH ($2.7 M_\odot$) viewed at an inclination of $i = 56^\circ$ (see Casares et al. 2022). For GX 339-4, the low FWHM value could be due to either a light BH or a low inclination (Heida et al. 2017). Since Fig. 1 is a representation of the mass function itself, it provides an efficient way to identify BHs. As is discussed in C18, BHs are easily selected above $\text{FWHM} \geq 2200 \text{ km s}^{-1}$ since CV intruders over this limit must have a short $P_{\text{orb}} \lesssim 2.1 \text{ h}$ (i.e. below the period gap) and are likely to be eclipsing. On the other hand, additional information (such as P_{orb}) is needed to clearly separate BHs from CVs below $\text{FWHM} \lesssim 2200 \text{ km s}^{-1}$.

Table 1. FWHM and EW of $H\alpha$ lines in quiescent BH XRTs.

Source	P_{orb} (d)	spectra (#)	epochs (#)	FWHM (km s^{-1})	EW (\AA)	References for P_{orb}
V404 Cyg	6.471170(2)	208	18	1012±94	24±5	(1)
BW Cir	2.54451(8)	98	4	1061±100	56±11	(2)
GX 339-4	1.7587(5)	1	1	855±52	76±12	(3)
XTE J1550-564	1.5420333(24)	34	2	1453±125	29±5	(4)
MAXI J1820+070	0.68549(1)	11	1	1678±85	75±19	(5)
N. Oph 77	0.5228(44)	4	4	1894±155	57±28	(6)
N. Mus 91	0.43260249(9)	88	5	1797±88	66±9	(7)
MAXI J1305-704	0.394(4)	1	1	2350 ±203	33±6	(8)
GS 2000+25	0.3440915(9)	2	2	2192±100	28±7	(9)
A 0620-00	0.32301415(7)	101	6	1938±94	58±12	(10)
XTE J1650-500 ^a	0.3205(7)	1	1	1898±121	9±2	(11), (12)
N. Vel 93	0.285206(1)	1	1	2055±124	63±10	(13)
N. Oph 93	0.278(8)	1	1	2267±194	89±15	(14)
XTE J1859+226	0.276(3)	48	4	2341±145	108±18	(15)
KY TrA	0.26(1)	4	1	2167±185	56±18	(16)
GRO J0422+32	0.2121600(2)	40	4	1478±55	289±39	(17)
XTE J1118+480	0.16993404(5)	131	6	2732±161	87±17	(18)
Swift J1753.5-0127	0.1358(8)	40	3	3502±145	166±17	(19)
Swift J1357.2-0933	0.106969(23)	70	3	4137±206	105±15	(20)
MAXI J1659-152	0.10058(22)	1	1	3309±361	130±23	(21)

References. (1) Casares et al. (2019); (2) Casares et al. (2009); (3) Heida et al. (2017); (4) Orosz et al. (2011); (5) Torres et al. (2019); (6) Harlaftis et al. (1997); (7) Wu et al. (2015); (8) Mata Sánchez et al. (2021); (9) Harlaftis et al. (1996); (10) González Hernández et al. (2017); (11) Sánchez-Fernández et al. (2002); (12) Orosz et al. (2004); (13) Filippenko et al. (1999); (14) Casares et al. (2023); (15) Yanes-Rizo et al. (2022); (16) Yanes-Rizo et al. (2024); (17) Webb et al. (2000); (18) González Hernández et al. (2017); (19) Yanes-Rizo et al. (2025); (20) Casares et al. (2022); (21) Kuulkers et al. (2013).

Notes.

^(a) FWHM and EW values obtained when the XRT was 1.4 mag brighter than full quiescence (Appendix A).

2.2. EW versus orbital period

In Fig. 2 we plot the behaviour of EWs versus P_{orb} for the same sample of BH XRTs and CVs as in Fig. 1. Again, the error bars for SDSS CV EWs are not shown as they are smaller than the symbol size. Realistic errors, including orbital and secular variability, are estimated at the $\approx 14\%$ level (see C15). Similar to the FWHM case, we observe that (i) EWs tend to increase with decreasing P_{orb} , and (ii) BH EWs are typically larger than CV EWs at the same P_{orb} . This is illustrated by the blue histogram, which represents the mean EW for CVs calculated in ten uniform bins of size $\Delta \log P_{\text{orb}} = 0.2$. Only XTE J1650-500 has an EW significantly below the CV mean for its P_{orb} , but as was mentioned earlier this is due to the fact that the spectra were obtained when the system had not yet reached true quiescence².

To understand the EW evolution with P_{orb} , we have built a toy model that generates synthetic EWs based on the Roche geometry and the continuum blackbody radiation associated with the donor star and the accretion disc. The $H\alpha$ emission is set to arise from the surface of the disc and it is assumed to be optically thin. A key ingredient of the model is the P_{orb} dependence of the donor effective temperature, which we have calibrated in Appendix B using eq. B.2. The latter was derived from a compilation of empirical spectral types of BH donors (Table B.1) and CV donors from Knigge (2006). In the case of BH binaries we

fixed $q = 0.06$ (Casares 2016, also Table B.3), while for CVs we adopted the aforementioned exponential increase with P_{orb} , i.e. $q = 0.73 - 11.55 \times \exp[-(P_{\text{orb}} + 0.39)/0.15]$. In the case of CVs, we also added an extra blackbody to account for the emission from the white dwarf. Further details of the modelling are given in Appendix C.

The black lines shown in Fig. 2 represent the BH EWs predicted by our model for three different inclinations: 33° , 60° , and 80° , i.e. the median and extremes containing 68 % of the values for an isotropic distribution of orientations. We observe that, despite the very rough approximations involved, our model is able to provide a qualitative description of the behaviour of the BH EWs with P_{orb} . Overall, the increase in BH EWs with decreasing P_{orb} is explained by the reduction in donor stellar flux caused by the drop in temperature, which becomes more pronounced at $P_{\text{orb}} < 0.3$ d (see Fig. B.1). As a consequence, the accretion disc becomes the dominant source of continuum light at $P_{\text{orb}} \lesssim 0.2$ d and, due to the foreshortening caused by binary inclination, a wider range of EW values is expected at these short orbital periods.

As is shown in Appendix C, the model is also able to reproduce the larger EWs observed in BHs simply by invoking their smaller q values (see Fig. C.2). This has the effect of reducing the relative contribution of the donor star to the continuum flux, increasing the EW of the $H\alpha$ line. Only at very short periods below the period gap ($P_{\text{orb}} \lesssim 0.085$ d) do CV mass ratios become comparable to the ones of BHs, but then the white dwarf contribution starts to dominate over the donor's continuum in the $H\alpha$ region, keeping the EW values of CVs below the EWs of BHs. Obviously the model is far too simplistic to explain the EW scatter

²Photometry performed on the acquisition image indicates that the system was 1.4 mags brighter than quiescence at the time of the spectroscopic observations (see Appendix A for details). Assuming a constant $H\alpha$ flux, this would imply that the quoted EW is underestimated by a factor of ≈ 3.6 .

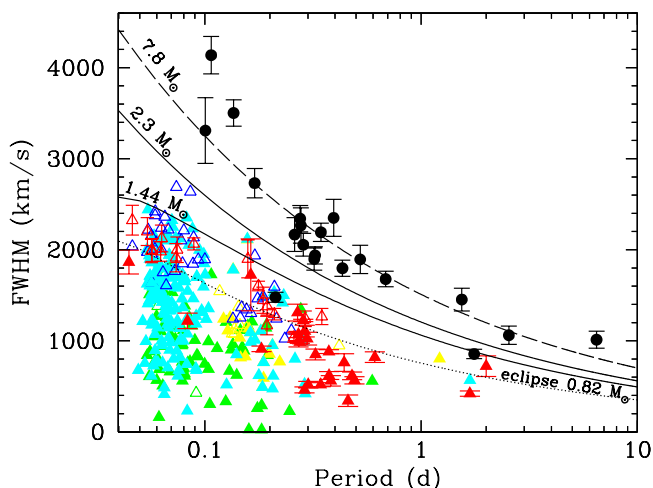


Fig. 1. Distribution of BH XRTs (black circles) and CVs (triangles) in the FWHM- P_{orb} plane. Open triangles indicate eclipsing CVs, while filled triangles non-eclipsing CVs. Red triangles represent 43 CVs from C15 and blue or cyan, green, and yellow triangles the 305 SDSS CVs of dwarf novae, magnetic, and nova-like types, respectively (Inight et al. 2003). For reference, we indicate the maximum FWHM for a Chandrasekhar-mass white dwarf viewed edge-on, and the lower limit of the FWHM for accretion disc eclipses of a typical $0.82 M_{\odot}$ CV white dwarf (dotted line). We also plot the maximum FWHM of a $2.3 M_{\odot}$ neutron star viewed edge-on. The expected track of a canonical $7.8 M_{\odot}$ BH seen at 60° inclination is represented by the dashed line.

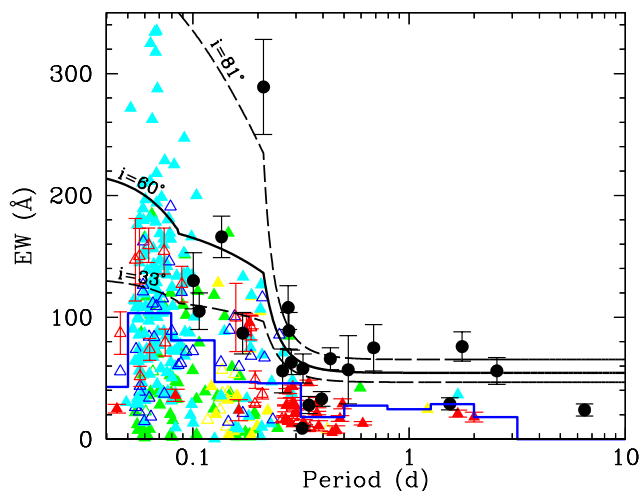


Fig. 2. EW versus P_{orb} for the same sample of BHs and CVs as in Fig. 1. For reference we plot BH EW lines of constant inclination ($i=33^{\circ}$, 60° and 80°), computed with our toy model simulation (see Appendix C for details). The blue histogram indicates the mean EW for CVs in ten period bins.

seen in systems with similar P_{orb} , mass ratios and inclinations. Different accretion disc structures and the intrinsic variability in the continuum and/or the $H\alpha$ flux (perhaps in response to irradiation, e.g. Hynes et al. 2002, 2004) are also likely to play an important role in the observed EW values.

We have so far avoided quiescent XRTs with neutron stars in this paper. This is because the number of systems with available quiescent FWHM and EW measurements is limited to Cen X-4 and XTE J2123-058 (see Table 3 in Casares 2015). A third obvious candidate, Aql X-1, is unfortunately contaminated by a very bright interloper (Chevalier et al. 1999; Mata Sánchez et al.

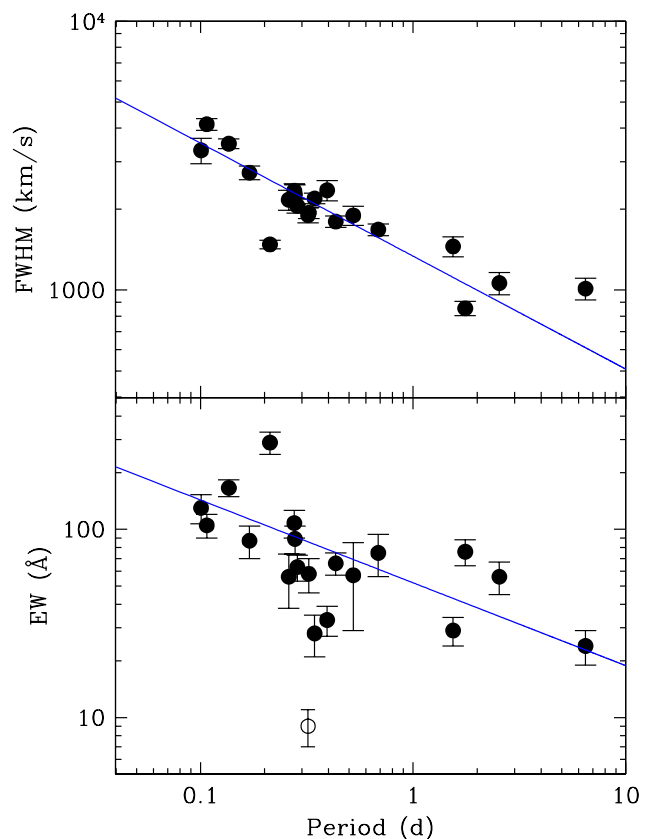


Fig. 3. Power-law fits to the orbital dependence of the FWHM and EW in quiescent BH XRTs. The EW of XTE J1650-400 (open circle) has been masked from the fit.

2017), which biases the EW and FWHM determination. Cen X-4 and XTE J2123-058 fall in regions of the P_{orb} -FWHM and P_{orb} -EW diagrams populated by CVs, and therefore cannot be unambiguously identified. This is not surprising given the comparable mass ratios and compact object masses of the two populations.

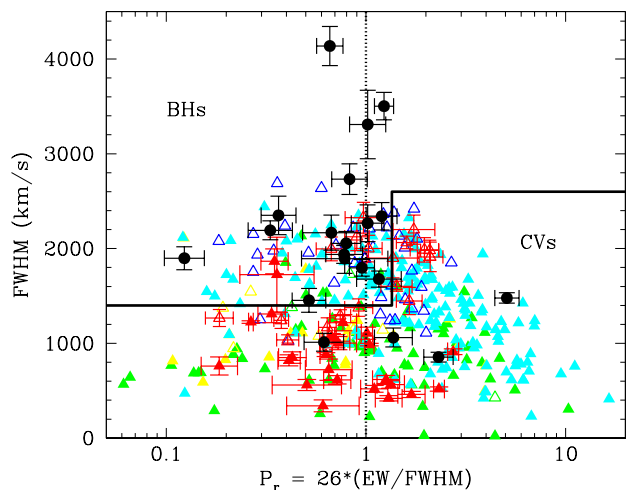
3. A $H\alpha$ metric for selecting quiescent BH XRTs

In this section we exploit the orbital period dependence of the FWHM and the EW of $H\alpha$ lines in BH XRTs to facilitate the selection of new dormant BHs. A least-squares power-law fit to the BH FWHM data versus P_{orb} yields $\text{FWHM} = 1337 P_{\text{orb}}^{-0.42}$, with FWHM expressed in units of kilometers per second and P_{orb} in days. The choice of a power law is physically motivated by the mass function equation, i.e. $\text{FWHM} \propto K_2 \propto P_{\text{orb}}^{-1/3}$. We have not considered the error bars in the fit to avoid this being dominated by points with a low FWHM, and thus small fractional errors. Similarly, a power-law fit to the EWs gives $\text{EW} = 52 P_{\text{orb}}^{-0.44}$, with EW in units of angstroms. Adopting other functional forms, such as an exponential decay or polynomial, does not lead to statistically improved fits. Here we have masked the extremely low EW outlier of XTE J1650-400 because the binary was not in true quiescence. Both power-law fits to the FWHM and EW BH values are shown in Fig. 3.

The previous expressions provide rough estimates of BH orbital periods based on FWHM and EW information alone. We refer to these as P_{FWHM} and P_{EW} , respectively. Given the scatter in the power-law fits, the difference between these estimates and

Table 2. BH selection against CV rejection using the P_r metric.

P_r	Selected BHs	Rejected CVs
0.10-10.0	85 %	57 %
0.30-3.33	75 %	62 %
0.50-2.00	65 %	72 %
0.60-1.66	60 %	80 %
0.74-1.35	50 %	89 %

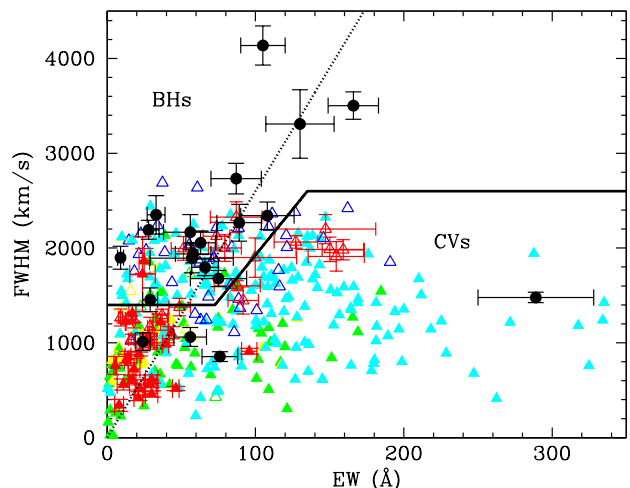

Fig. 4. Diagram showing the distribution of BHs and CVs in the FWHM- P_r plane. The same symbol code is used as in Figs. 1 and 2. Vertical dots mark the BH clustering line, while the thick solid lines delineate the optimal region for separating BHs from CVs.

the true P_{orb} can be significant. However, since both P_{FWHM} and P_{EW} are expected to track P_{orb} better in BHs than in CVs, we decided to choose the ratio $P_r \equiv (P_{\text{FWHM}}/P_{\text{EW}})^{0.43}$ as a suitable metric for BH selection, which we now approximate as $P_r \approx 26 (EW/FWHM)$. Figure 4 depicts P_r against FWHM for our BHs and the ensemble of CVs.

Since BHs are expected to cluster around $P_r \approx 1$, it thus seems convenient to choose vertical bands of different widths, centred at $P_r = 1$, to optimise their selection against CVs. As is shown in Table 2, the narrower the band the more CVs are rejected, but this comes at the cost of selecting fewer BHs too. Interestingly, the distribution of BHs appears to be skewed towards lower P_r values, with very few BHs also found under $\text{FWHM} = 1400 \text{ km s}^{-1}$. Furthermore, dynamical arguments based on the Chandrasekhar mass limit indicate that CVs cannot produce $H\alpha$ lines broader than $\approx 2600 \text{ km s}^{-1}$ (see Fig 1, also C15). Given the above constraints, we propose an optimal region for BH selection defined by the limits $\text{FWHM} > 1400 \text{ km s}^{-1}$ for $P_r < 1.35$ and $\text{FWHM} > 2600 \text{ km s}^{-1}$ for $P_r > 1.35$. These cuts are shown in Figure 4 and allow one to select 80 % of the current sample of BHs, while rejecting 77 % of the CVs. It is worth noting that at least 33 % of the non-rejected CVs are eclipsing³ and therefore easily identified by light curve variability. It should also be mentioned that the mere detection of eclipses provides us with P_{orb} information and thus, when combined with FWHM values, mass functions that constrain the nature of the compact star.

Figure 5 displays the P_r metric in the simpler EW-FWHM plane. Here the BHs tend to cluster around $\text{FWHM}/\text{EW} = 26$ (dot-

³Other non-rejected SDSS CVs may also be eclipsing, but have not yet been confirmed due to insufficient photometric coverage.


Fig. 5. Distribution of BHs and CVs in the FWHM-EW plane. The BH clustering line at $\text{FWHM} = 26 \times \text{EW}$ is indicated by dots, while the solid line marks our Fig. 4 cuts for optimal BH selection.

ted line in Fig 5), while the previous selection cuts are represented by the solid lines defined by

$$\begin{aligned}
 & \text{FWHM} > 1400 & \text{EW} < 73 \\
 & \text{FWHM} > 19.3 \times \text{EW} & 73 < \text{EW} < 135, \\
 & \text{FWHM} > 2600 & \text{EW} > 135
 \end{aligned} \tag{1}$$

with the FWHM expressed in units of kilometers per second and EW in angstroms.

Obviously, the proposed cuts are based on a limited number of BHs and should be considered as preliminary. In any case, they can help to discover new dormant BHs under the $\text{FWHM} \approx 2200 \text{ km s}^{-1}$ limit proposed in C18. The diagnostics presented here will prove useful for current and future synoptic spectroscopic surveys (e.g. LAMOST, 4MOST, WEAVE), in which large numbers of spectra will be collected. It will also benefit blind photometric surveys, such as $H\alpha$ WKS and its pathfinder (Mini- $H\alpha$ WKS), which have been tailored to extract EW and FWHM information from $H\alpha$ -emitting objects (C18). Nevertheless, CVs have an estimated Galactic density of $\sim 10^4 \text{ kpc}^{-3}$ (Pala et al. 2020) and are thus ≈ 1000 times more abundant than BH XRTs (Corral-Santana et al. 2016). This implies that, assuming similar absolute magnitudes and galactic distributions, our FWHM-EW cuts would still select ≈ 300 intruding CVs per BH. Clearly, additional information from other multi-frequency surveys will be crucial for unveiling BH imposters and refining selection diagnostics. In particular, the absence of blue/UV excess in UVEX/Galex colours (a signature of a white dwarf or disc boundary layer; e.g. Gänsicke et al. 2009), will strengthen the possibility that new candidates are authentic dormant BH XRTs. Ultimately, these will need to be confirmed by dedicated follow-up spectroscopic studies.

A related question is whether FWHM and/or EW information can be used to distinguish BH XRTs that are undergoing some level of accretion activity from truly quiescent systems, even if X-rays are not detected. BH XRTs are known to follow a distinct FWHM and EW pattern as they transition from outburst to quiescence. Many examples in the literature consistently show that outburst spectra evolve from being almost featureless (sometimes with weak $H\alpha$ emission embedded in broad absorptions) to developing increasingly stronger and broader $H\alpha$ lines. For example, during the decay of the A0620-00 discovery outburst,

the EW increased from ~ 5.8 to 14 \AA and FWHM from ~ 1100 to 1830 km s^{-1} between Sept 1975 and May 1976 (Whelan et al. 1977). Other studies, focusing on the late outburst decline, suggest that the FWHM tends to approach quiescent values faster than the EW. For example, from November 2000 to April 2001, XTE J1118+480 promptly reached the quiescent FWHM value at $\approx 2700 \text{ km s}^{-1}$, while the EWs showed a monotonic increase between 14 and 44 \AA , still far from the $\approx 87 \text{ \AA}$ quiescent value (Zurita et al. 2002a; Torres et al. 2004). In view of this, it seems tempting to conclude that $H\alpha$ EWs are a more sensitive diagnostic of disc activity than FWHMs and could perhaps be used to detect unusual disc activity or even precursors to new outbursts. Interestingly, a chance spectrum of V404 Cyg obtained 13 h before the X-ray trigger of the 2015 outburst revealed that the EW of the $H\alpha$ line was ~ 15 times larger than in quiescence, while the FWHM was almost unchanged (Bernardini et al. 2016; Casares et al. 2019).

4. Conclusions

1. We have compiled FWHM and EW values of $H\alpha$ emission lines in a sample of 20 quiescent BH XRTs. The BH collection typically covers multiple epochs of quiescence, sometimes spanning several decades. Despite evidence of orbital and secular variability, the mean FWHM and EW values are found to be rather stable (Appendix A). The BH FWHM and EW values have been compared with the ones of a sample of 353 CVs (305 from SDSS I to IV) with known orbital periods.
2. Our compilation shows that both FWHM and EW values decrease with P_{orb} , while, for a given P_{orb} , they tend to be larger in BHs than in CVs.
3. The larger BH FWHMs are a natural consequence of their higher compact object masses. The larger EWs, on the other hand, could be explained by a lower level of continuum flux. This stems from a combination of extreme mass ratios (which limit the relative contribution of the companion to the total flux) and the absence of a white dwarf continuum.
4. Furthermore, we derive an empirical $P_{\text{orb}} - T_{\text{eff}}$ relation for companion stars in BH XRTs, which is also valid for CVs (Appendix B). From this we infer that the companion is the main source of $H\alpha$ continuum flux above ≈ 0.2 d, while the accretion disc dominates otherwise. In the case of CVs, the white dwarf also contributes to the diluting continuum (especially at $P_{\text{orb}} \lesssim 0.085$ d), further capping EW values with respect to BHs.
5. We finally present a tentative metric ($P_r = 26 \text{ EW}/\text{FWHM}$) for detecting dormant BHs, based on the period dependence of the FWHM and EW in BH XRTs. We find that selection cuts defined by $\text{FWHM} > 1400 \text{ km s}^{-1}$ for $P_r < 1.35$ and $\text{FWHM} > 2600 \text{ km s}^{-1}$ for $P_r > 1.35$ allow us to filter out $\approx 77 \%$ of CVs, while still retaining $\approx 80 \%$ of our sample of BHs. In any case, given the high Galactic density of CVs, the proposed metric needs to be combined with other multi-frequency diagnostics for an efficient selection of dormant BH XRTs.

Acknowledgements. We thank the anonymous referee for useful and constructive comments that helped improve the manuscript. JC and MAPT acknowledge support by the Spanish Ministry of Science via the Plan de Generación de Conocimiento through grants PID2022-143331NB-I00 and PID2021-124879NB-I00, respectively. SNU is supported by the FPI grant PREP2022-000508, also under program PID2022-143331NB-I00. We thank Keith Inight for sharing his database of SDSS CV spectra with us, and Cynthia Froning for sharing the SED data on A0620-00. We also thank Rosa Clavero, David Jones and other members of the IAC team of support astronomers for undertaking the

2016-2021 NOT observations of V404 Cyg during Service time. We dedicate this paper to the memory of Tom Marsh, creator of the molly software and a beacon in the field of compact binaries.

References

- Abbott B.P., Abbott, R., Abbott, T.D., et al. 2019, *ApJ*, 882, L24
 Arur, K., & Maccarone, T.J. 2018, *MNRAS*, 474, 69
 Baglio, M.C., Russell, D.M., Alabarta, K., et al. 2023, *ATel.*, 16192, 1
 Beer, M.E., & Podsiadlowski, P. 2002, *MNRAS*, 331, 351
 Bellm, E.C., Wang, Y., van Roestel, J., et al. 2023, *ApJ*, 956, 21
 Bernardini, F., Russell, D.M., Shaw, A.W., et al. 2016, *ApJ*, 818, L5
 Bertelli, G., Girardi, L., Marigo, P., & Nasi, E. 2008, *A&A*, 484, 815
 Bertelli, G., Nasi, E., Girardi, L., & Marigo, P. 2009, *A&A*, 508, 355
 Burdge, K.B., El-Badry, K., Kara, E., et al. 2024, *Nature*, 635, 316
 Buxton, M., & Vennes, S. 2001, *PASA*, 18, 91
 Callanan, P.J., & Charles, P.A. 1991, *MNRAS*, 249, 573
 Calvelo, D.E., Vrtilek, S.D., Steeghs, D., et al. 2009, *MNRAS*, 399, 539
 Cantrell, A.G., Bailyn, C.D., McClintock, J.E., & Orosz, J.A., 2008, *ApJ*, 673, L159
 Cantrell, A.G., Bailyn, C.D., Orosz, J.A., et al., 2010, *ApJ*, 710, 1127
 Casares, J. 1996, *Astrophysics and Space Science Library*, Proc. of the 158th coll. of IAU, ed. A. Evans & J.H. Wood, Dordrecht: Kluwer Academic Publishers, Vol. 208, p.395
 Casares, J. 2015, *ApJ*, 808, 80
 Casares, J. 2016, *ApJ*, 822, 99
 Casares, J. 2018, *MNRAS*, 473, 5195
 Casares, J., & Charles, P.A. 1994, *MNRAS*, 271, L5
 Casares, J., & Torres, M.A.P. 2018, *MNRAS*, 481, 4372
 Casares, J., Charles, P.A., Naylor, T., & Pavlenko, E.P. 1993, *MNRAS*, 265, 834
 Casares, J., Charles, P.A., & Marsh, T.R., 1995a, *MNRAS*, 277, L45
 Casares, J., Martin, A.C., Charles, P.A., et al. 1995b, *MNRAS*, 276, L35
 Casares, J., Orosz, J.A., Zurita, C., et al. 2009, *ApJS*, 181, 238
 Casares, J., Martín, E.L., Charles, P.A., Molero, P., & Rebolo, R. 1997, *New A*, 1, 299
 Casares, J., Zurita, C., Shahbaz, T., Charles, P.A., & Fender, R.P. 2004, *ApJ*, 613, L133
 Casares, J., Orosz, J.A., Zurita, C., et al. 2009, *ApJS*, 181, 238
 Casares, J., Muñoz-Darias, T., Mata Sánchez, D., et al. 2019, *MNRAS*, 488, 1356
 Casares, J., Torres, M.A.P., Muñoz-Darias, et al. 2022, *MNRAS*, 516, 2023
 Casares, J., Yanes-Rizo, I.V., Torres, M.A.P., et al. 2023, *MNRAS*, 526, 5209
 Chevalier, C., Ilovaisky, S.A., Leisy, P., & Patat, F. 1999, *A&A*, 347, L51
 Ciatti, F., & Vittone, A. 1977, *IBVS* N. 1261
 Corral-Santana, J.M., Casares, J., Shahbaz, T., et al. 2011, *MNRAS*, 413, L15
 Corral-Santana, J.M., Casares, J., Muñoz-Darias, T., et al., 2013, *Science*, 339, 1048
 Corral-Santana, J.M., Casares, J., Muñoz-Darias, T., Bauer, F.E., Martínez-Pais, I.G. & Russell, D.M. 2016, *A&A*, 587, A61
 Corral-Santana, J.M., Torres, M.A.P., Shahbaz, T., et al. 2018, *MNRAS*, 475, 1036
 Drilling, J.S., & Landolt, A.U. 2002, *Normal Stars in Allen's Astrophysical Quantities*, ed. A.N. Cox, Springer New York, NY, p. 381, ISBN 978-0-387-95189-8
 Eggleton, P.P. 1983, *ApJ*, 268, 368
 Filippenko, A.V., Matheson, T., & Barth, A.J. 1995, *ApJ*, 455, L139
 Filippenko, A.V., Leonard, D.C., Matheson, T., et al. 1999, *PASP*, 111, 969
 Filippenko, A.V., Leonard, D.C., Matheson, T., et al. 1999, *PASP*, 111, 969
 Frank, J., King, A.R., & Raine, D.J. 2002, *Accretion Power in Astrophysics*, Vol. 21 (3rd ed.; Cambridge: Cambridge Univ. Press)
 Froning, C.S., Robinson, E.L., & Bitner, M.A. 2007, *ApJ*, 663, 1215
 Froning, C.S., Cantrell, A.G., Maccarone, T.J., et al. 2011, *ApJ*, 743, 26
 Gaia Collaboration, et al. 2024, *A&A*, 686, L2
 Gandhi, P., Rao, A., Johnson, M.A.C., Paice, J.A., & Maccarone, T.J. 2019, *MNRAS*, 485, 2642
 Gandhi, P., Rao, A., Charles, P.A., et al. 2020, *MNRAS*, 496, L22
 García, M.R., & Wilkes, B.J. 2002, *ATel.*, 104, 1
 García, M.R., Callanan, P.J., McClintock, J.E., & Zhao, P. 1996, *ApJ*, 460, 932
 Gänsicke, B.T., Dillon, M., Southworth, J., et al. 2009, *MNRAS*, 397, 2170
 Gelino, D.M., Harrison, T.E., & Orosz, J.A. 2001, *AJ*, 122, 2668
 Gelino, D.M., & Harrison, T.E. 2003, *ApJ*, 599, 1254
 Gelino, D.M., Balman, Ş., Kızıloğlu, Ü., et al. 2006, *ApJ*, 642, 438
 González Hernández J.I., Rebolo, R., Israelian, G., et al. 2004, *ApJ*, 609, 988
 González Hernández J.I., Rebolo, R., Israelian, G., et al. 2006, *ApJ*, 644, L49
 González Hernández J.I., Rebolo, R., & Israelian, G. 2008a, *A&A*, 478, 203
 González Hernández, J.I., Rebolo, R., Israelian, G., et al. 2008b, *ApJ*, 679, 732
 González Hernández J.I., & Casares J., 2010, *A&A*, 516, A58
 González Hernández J.I., Casares J., Rebolo, R., et al. 2011, *ApJ*, 738, 95
 González Hernández J.I., Rebolo, R., & Casares, J. 2012, *ApJ*, 744, L25

- González Hernández J.I., Rebolo, R., & Casares, J. 2014, MNRAS, 438, L21
- González Hernández J.I., Suárez-Andrés, L., Rebolo, R., & Casares, J. 2017, MNRAS, 465, L15
- Harlaftis, E.T., Horne, K., & Filippenko, A.V. 1996 PASP, 108, 762
- Harlaftis, E.T., Steeghs, D., Horne, K., & Filippenko, A.V. 1997 AJ, 114, 1170
- Harlaftis, E.T., Collier, S., Horne, K., & Filippenko, A.V. 1999 A&A, 341, 491
- Harlaftis, E.T., & Greiner, J. 2004, A&A, 414, L13
- Harrison, T.E., Howell, S.B., Szkody, P., & Cordova, F.A. 2007, AJ, 133, 162
- Haswell, C.A., Hynes, R.I., King, A.R., & Schenker, K. 2002, MNRAS, 332, 928
- Heida, M., Jonker, P.G., Torres, M.A.P., & Chiavassa, A. 2017, ApJ, 846, 132
- Hynes, R.I., Zurita, C., Haswell, C.A., et al. 2002, MNRAS, 330, 1009
- Hynes, R.I., Charles, P.A., Garcia, M.R., et al. 2004, ApJ, 611, L125
- Hynes, R. I.; Bradley, C. K.; Rupen, M., et al. 2009, MNRAS, 399, 2239
- Hynes, R. I. & Robinson, E.L. 2012, ApJ, 749, 3
- Inight, K., Gänsicke, B.T., Breedt, E., et al. 2023, MNRAS, 524, 4867
- Israelián, G., Rebolo, R., Basri, G., Casares, J., & Martín, E.L. 1999, Nature, 401, 142
- Jonker, P.G., Kaur, K., Stone, N., & Torres, M.A.P. 2021, ApJ, 921, 131
- Khargharia, J., Froning, C.S., & Robinson E.L. 2010, ApJ, 716, 1105
- Khargharia, J., Froning, C.S., Robinson, E.L., & Gelino, D.M. 2013, AJ, 145, 21
- King, A.R. 1993, MNRAS, 260, L5
- King, A.R., Kolb, U., & Burderi, L. 1996, ApJ, 464, L127
- King, N.L., Harrison, T.E., & McNamara, B.J. 1996, AJ, 111, 1675
- Kneivitt, G., Wynn, G.A., Vaughan, S. & Watson, M.G. 2014, MNRAS, 437, 3087
- Knigge, C. 2006, MNRAS, 373, 484
- Koljonen, K.I.I., Russell, D.M., Corral-Santana, J.M., et al. 2016, MNRAS, 460, 942
- Kreidberg, L., Baily, C.D., Farr, W., & Kalogera, V. 2012, ApJ, 757, 36
- Kuulkers, E., Kouveliotou C., Belloni, T., et al. 2013, A&A, 552, A32
- Lin, J., Yan, Z., Han, Z., & Yu, W. 2019, ApJ, 870, 126
- Littlefair, S., Dhillon, V.S., Marsh, T.R., & Gänsicke, B.T. 2006, MNRAS, 371, 1435
- Maccarone, T.J., & Patruno, A., 2013 MNRAS, 428, 1335
- Macias, P., Orosz, J.A., Baily, C.D., et al. 2011, Bulletin of the American Astronomical Society, Vol. 43, 2011
- Marsh, T.R., Robinson, E.L., & Wood, J.H. 1994, MNRAS, 266, 137
- Mata Sánchez, D., Muñoz-Darias, T., Casares, J., Corral-Santana, J.M., & Shahbaz, T. 2015, MNRAS, 454, 2199
- Mata Sánchez, D., Muñoz-Darias, T., Casares, J., & Jiménez Ibarra, F. 2017, MNRAS, 464, L41
- Mata Sánchez, D., Rau, A., Álvarez-Hernández, A., et al. 2021, MNRAS, 506, 581
- Menou, K., Narayan, R., & Lasota, J.-P. 1999, ApJ, 513, 811
- McClintock, J.E., & Remillard, R.A. 1986, ApJ, 308, 110
- McClintock, J.E., Horne, K., & Remillard, R.A. 1995, ApJ, 442, 358
- McClintock, J.E., Garcia, M.R., Caldwell, N., et al. 2001, ApJ, 551, L147
- McClintock, J.E., Narayan, R., Garcia, M.R., et al. 2003, ApJ, 593, 435
- Murdin, P., Griffiths, R.E., Pounds, K.A., Watson, M.G., & Longmore, A.J. 1977, MNRAS, 178, 27
- Murdin, P., Allen, D.A., Morton, D.C., Whelan, J.A.J., & Thomas, R.M. 1980, MNRAS, 192, 709
- Naoz, S., Fragos, T., Geller, A., et al. 2016, ApJ, 822, L24
- Narayan, R., & McClintock, J.E. 2005, ApJ, 623, 1017
- Neilsen, J., Steeghs, D., & Vrtilik, S.D. 2008, MNRAS, 384, 849
- Oke, J.B. 1977, ApJ, 217, 181
- Orosz, J.A. 2003, in A Massive Star Odyssey, from Main Sequence to Supernova, Proc. of IAU Symp., ed. K. van der Hucht, A. Herrero, & C. Esteban (San Francisco: Astronomical Society of the Pacific) Vol 212, p. 3650
- Orosz, J.A., & Bailyn, C.D. 1995, ApJ, 446, L59
- Orosz, J.A., & Bailyn, C.D. 1997, ApJ, 477, 876
- Orosz, J.A., Bailyn, C.D., Remillard, R.A., McClintock, J.E., & Foltz, C.B. 1994, ApJ, 436, 848
- Orosz, J.A., Bailyn, C.D., McClintock, J.E., & Remillard, R.A. 1996, ApJ, 468, 380
- Orosz, J.A., Jain, R.K., Bailyn, C.D., McClintock, J.E., & Remillard, R.A. 1998, ApJ, 499, 375
- Orosz, J.A., Kuulkers, E., van der Klis, M., et al. 2001, ApJ, 555, 489
- Orosz, J.A., Groot, P.J., van der Klis, M., et al. 2002, ApJ, 568, 845
- Orosz, J.A., McClintock, J.E., Remillard, R.A., & Corbel, S. 2004, ApJ, 616, 376
- Orosz, J.A., Steiner, J.F., McClintock, J.E., et al. 2011, ApJ, 730, 75
- Özel, F., Psaltis, D., Narayan, R., & McClintock, J.E. 2010, ApJ, 725, 1918
- Paczynski B., 1971, ARA&A, 9, 183
- Pala, A.F., Gänsicke, B.T., Breedt, E., et al. 2020, MNRAS, 494, 3799
- Pecauti, M.J., & Mamajek, E.E. 2013, ApJS, 208, 9
- Peterson, B.M., Ferrarese, L., Gilbert, K.M., et al. 2004, ApJ, 613, 682
- Podsiadlowski, Ph., Rappaport, S., & Pfahl, E.D. 2002, ApJ, 565, 1107
- Podsiadlowski, Ph., Rappaport, S., & Han, Z. 2003, MNRAS, 341, 385
- Poutanen, J., Veledina, A., Berdyugin, A.V., et al. 2022, Science, 375, 874
- Pylyser, E., & Savonije, G.J. 1988, A&A, 191, 57
- Remillard, R.A., McClintock, J.E., & Bailyn, C.D. 1992, ApJ, 399, L145
- Remillard, R.A., Orosz, J.A., McClintock, J.E., & Bailyn, C.D. 1996, ApJ, 459, 226
- Ritter, H., & Kolb, U. 2003, A&A, 404, 301
- Ruiz, M., Shapiro, S.L., & Tsokaros, A. 2018, *PhRvD*, 97, 021501
- Russell, D.M., Lewis, F., & Gandhi, P. 2017, ATel., 10797, 1
- Russell, D.M., Qasim, A.A., Bernardini, F., et al. 2018, ApJ, 852, 90
- Saikia, P., Russel, D.M., Baglio, M.C., et al. 2022, ApJ, 932, 38
- Savoury, C.D.J., Littlefair, S.P., Dhillon, V.S., et al. 2011, MNRAS, 415, 2025
- Sánchez-Fernández, C., Zurita, C., Casares, J., et al. 2002, IAUCirc 7989
- Shahbaz, T., van der Hooft, F., Charles, P.A., Casares, J., & van Paradijs, J. 1996, MNRAS, 282, L47
- Shahbaz, T., Bandyopadhyay, R.M., & Charles, P.A. 1999a, A&A, 346, 82
- Shahbaz, T., van der Hooft, F., Casares, J., Charles, P.A., & van Paradijs, J. 1999b, MNRAS, 306, 89
- Shahbaz, T., Russell, D.M., Zurita, C., et al. 2013, MNRAS, 434, 2696
- Shibata, M., Zhou, E., Kiuchi, K., et al. 2019, *PhRvD*, 100, 023015
- Siegel, J.C., Kiato, I., Kalogera, V., et al. 2023, ApJ, 954, 212
- Smith, D.A., & Dhillon V.S. 1998, MNRAS, 301, 767
- Steeghs, D., McClintock, J.E., Parsons, S.G., et al. 2013, ApJ, 768, 185
- Thorstensen, J.R., Fenton, W.H., Patterson, J.O., et al. 2002a, ApJ, 567, L49
- Thorstensen, J.R., Fenton, W.H., Patterson, J.O., et al. 2002b, PASP114, 1117
- Torres, M.A.P., Callanan, P.J., Garcia, M.R., et al. 2004, ApJ, 612, 1026
- Torres, M.A.P., Jonker, P.G., Miller-Jones, J.C.A., et al. 2015, MNRAS, 450, 4292
- Torres, M.A.P., Casares, J., Jiménez-Ibarra, F., et al. 2019, ApJ, 882, L21
- Torres, M.A.P., Casares, J., Jiménez-Ibarra, F., et al. 2020, ApJ, 893, L37
- Torres, M.A.P., Jonker, P.G., Casares, J., Miller-Jones, J.C.A., & Steeghs, D. 2021, MNRAS, 501, 2174
- van Belle, G.T., Lane, B.F., Thompson, R.R., et al. 1999, AJ, 117, 521
- Wagner, R.M., Foltz, C.B., Shahbaz, T., et al. 2001, ApJ, 556, 42
- Webb, N.A., Naylor, T., Ioannou, Z., Charles, P.A., & Shahbaz, T. 2000, MNRAS, 317, 528
- Webbink, R.F., Rappaport S.A., & Savonije, G.J. 1983, ApJ, 270, 678
- Whelan, J.A.J., Ward, M.J., Allen, D.A., et al. 1977, MNRAS, 180, 657
- Wu, Y.X., Yu, W., Li, T.P., Maccarone, T.J., & Li, X.D. 2010, ApJ, 718, 620
- Wu, J., Orosz, J.A., McClintock, J.E., et al. 2015, ApJ, 806, 92
- Yanes-Rizo, I.V., Torres, M.A.P., Casares, J., et al. 2022, MNRAS, 517, 1476
- Yanes-Rizo, I.V., Torres, M.A.P., Casares, J., et al. 2024, MNRAS, 527, 5949
- Yanes-Rizo, I.V., Torres, M.A.P., Casares, J., et al. 2025, A&A, 694, A119
- Zhang, G., Russell, D.M., Bernardini, F., Gelfand, J.D., & Lewis, F. 2017, ATel., 10562, 1
- Zheng, W.-M., Wu, Q., Wu, J., et al. 2022, ApJ, 925, 83
- Zorotovic, M., Schreiber, M.R., & Gänsicke, B.T. 2011, A&A, 536, A42
- Zurita, C., Casares J., Shahbaz T., et al. 2002a, MNRAS, 333, 791
- Zurita, C., Sánchez-Fernández, C., Casares, J., et al. 2002b, MNRAS, 334, 999
- Zurita, C., Casares, J., Martínez-Pais, I.G., et al. 2002c, IAUC 7868
- Zurita, C., Torres, M.A.P., Steeghs, D., et al. 2006, ApJ, 644, 432
- Zurita, C., Corral-Santana, J.M., & Casares, J. 2015, MNRAS, 454, 3351
- Zurita, C., González Hernández J.I., Escorza, A., & Casares J., 2016, MNRAS, 460, 4289

Appendix A: An extensive collection of FWHM and EW values of $H\alpha$ lines in quiescent BH XRTs

We have assembled a new database of $H\alpha$ spectra of quiescent BH XRTs obtained in different epochs over 30 years. The present collection contains and supersedes the one reported in C15 and is presented in Table A.1. Listed references correspond to the papers where the original spectra were first reported and/or analysed. The spectra were obtained with a variety of telescopes: the 10.4 m Gran Telescopio Canarias (GTC), the 10 m Keck telescope, the 8.2 m Very Large Telescope (VLT), the 6.5 m Magellan Clay telescope, the 4.2 m William Herschel Telescope (WHT), the 4 m Victor M. Blanco telescope, the 3.9 m Anglo Australian Telescope (AAT), the 3.5 m New Technology Telescope (NTT), the 2.5 m Isaac Newton Telescope (INT), the 2.56 m Nordic Optical Telescope (NOT) and the 2.1 m telescope at the Observatorio de San Pedro Mártir (SPM). Some data have not yet been published and will be reported elsewhere. These are the 2019-2021 NOT and 2022 INT epochs of V404 Cyg, the 2023 GTC epoch of MAXI J1820+070, the 2019 GTC epoch of XTE J1859+226 and the 2017 GTC epoch of GRO J0422+32.

We consider BH XRTs to be in true quiescence when there is no sign of X-ray activity (i.e. outbursts, mini-outbursts or re-flares) and the optical flux remains consistent with the lowest measured values. To demonstrate that the selected spectra meet these criteria, we give in Table A.2 the dates of the quiescent periods relevant to our data. The listed magnitudes refer either to the start of quiescence, to a time average or to a range of values reported over the entire period. As can be seen in Table A.2, all the spectra correspond to quiescent epochs, including GX 339-4, which experienced a prolonged period of very low optical brightness in 2016 (Russell et al. 2017). The only exception is XTE J1650-500, as the spectroscopy of Sánchez-Fernández et al. (2002) was obtained approximately two months before the first quiescent magnitudes were reported (García & Wilkes 2002). To confirm this, we have performed PSF photometry on the acquisition images obtained by Sánchez-Fernández et al. (2002), finding $R=20.67\pm 0.04$, i.e. 1.4 mag brighter than the deepest magnitude available (García & Wilkes 2002). To further test whether the latter corresponds to true quiescence, we also performed PSF photometry on a Sloan r-band image from the DECaPS survey⁴, obtained on 29 April 2017 under good seeing conditions (0.78"). We found $r'=22.10\pm 0.12$, which is in good agreement with García & Wilkes (2002).

Following C15, we measured the FWHM of the $H\alpha$ line by fitting a Gaussian profile plus a constant in a window of $\pm 10,000$ km s⁻¹ centred at 6563 Å, after masking the neighboring He I $\lambda 6678$ line. The Gaussian model was previously degraded to the instrumental resolution of each spectrum, and the continuum level was rectified by fitting a low-order polynomial. Likewise, EW values were obtained by integrating the $H\alpha$ flux in the continuum normalised spectra. The entire spectral analysis was performed using routines within the MOLLY package⁵. Where possible, FWHM and EW values were measured from single individual spectra (e.g. V404 Cyg). When the quality of individual spectra was too poor FWHM and EW measurements were obtained from averaged spectra (e.g. MAXI J1659-152). In some cases, an orbitally averaged spectrum was kindly provided by the corresponding authors (e.g. GX 339-4) while in others we had to

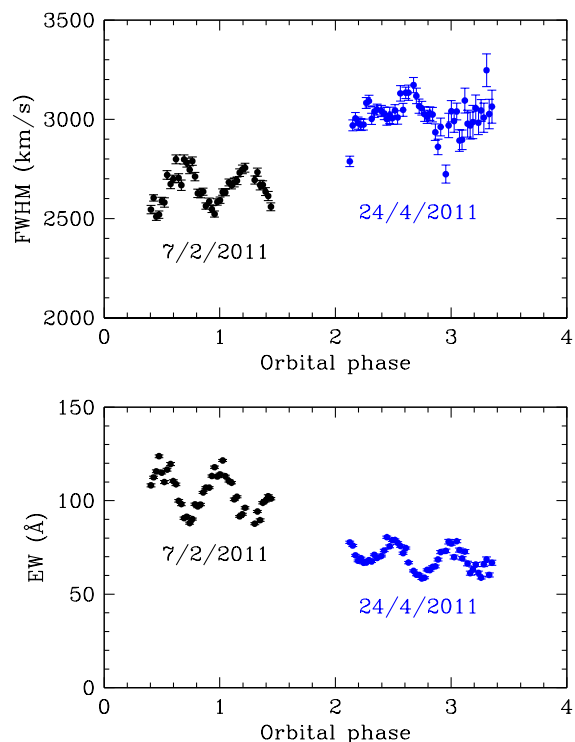


Fig. A.1. Orbital variation of FWHM and EW in XTE J1118+480 on the nights of February 7 and April 24 2011.

digitise averaged spectra from figures in the relevant papers (e.g. the WHT 1991-1992 epoch of A0620-00). The uncertainties introduced by the latter process are negligible compared to orbital and long-term variations typically observed in FWHM and EW.

Figure A.1 shows examples of orbital variability in the FWHM and EW values of XTE J1118+480 at two different epochs. Both parameters describe a double sine wave on each orbital cycle. The EW variations reflect changes in the optical continuum, driven by the ellipsoidal modulation of the companion star (e.g. Marsh et al. 1994). On the other hand, the phasing of the FWHM variations (i.e. minima at phases 0.4 and 0.9) indicate that these are likely caused by the motion of the hot-spot⁶ across the $H\alpha$ profile. Consequently, when only one spectrum is available in a given epoch (e.g. the Keck 2004 spectrum of XTE J1118+480) or its phase coverage is very limited (e.g. the WHT 1993 epoch of V404 Cyg), statistical uncertainties in FWHM and EW measurements were increased by adding quadratically a systematic error to account for the effect of orbital variability. We call these 'orbital' systematic errors $\sigma(\text{FWHM})_{\text{orb}}$ and $\sigma(\text{EW})_{\text{orb}}$, respectively.

To estimate $\sigma(\text{FWHM})_{\text{orb}}$ and $\sigma(\text{EW})_{\text{orb}}$, we focus on 24 epochs of 10 BHs with ≥ 50 % orbital coverage. In principle, one might expect $\sigma(\text{FWHM})_{\text{orb}}$ and $\sigma(\text{EW})_{\text{orb}}$ to depend on geometrical effects, different accretion disc structures or mass accretion rates. However, we see no evidence for a trend in the amplitude of the FWHM and EW variability with fundamental parameters such as binary inclination and P_{orb} , a proxy for mass

⁴Images are publicly available at <http://decaps.skymaps.info/>

⁵Molly was written by T. R. Marsh and is available from <https://cygnus.astro.warwick.ac.uk/phsaap/software/molly/html/INDEX.html>.

⁶In semi-detached binaries with an accreting compact star a hot-spot is formed by the collision of the gas stream with the outer accretion disc. For extreme mass ratios, characteristic of BH XRTs, the hot-spot crosses the observer's line of sight at orbital phases ≈ 0.4 and 0.9 , with phase 0 defined as the inferior conjunction of the mass donor star.

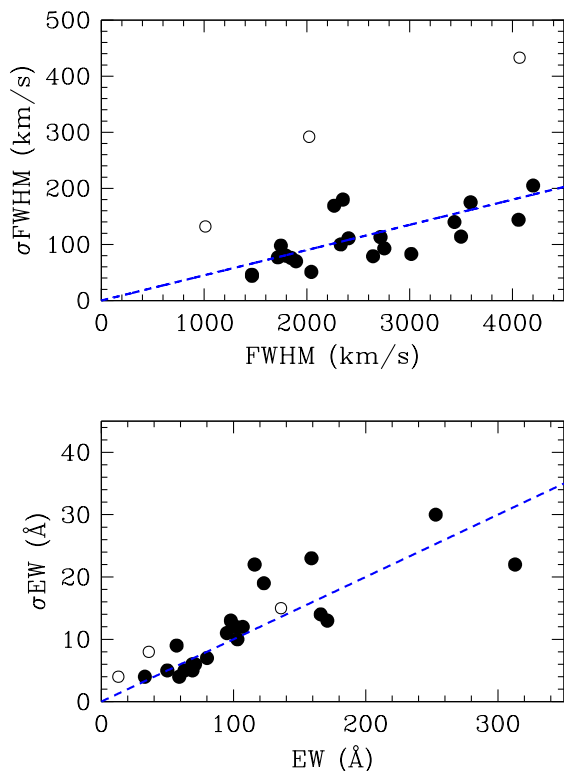


Fig. A.2. Orbital variability of FWHM (upper panel) and EW (lower panel) for 24 epochs of 10 BH XRTs with $\geq 50\%$ orbital coverage. Open circles mark the three epochs with $S/N \leq 3$ spectra and thus dominated by statistical noise. The dashed blue lines show linear fits to the data.

transfer rate. Conversely, Fig. A.2 shows that the amplitude of the variability increases with the mean value, with a linear fit giving $\sigma(\text{FWHM})_{\text{orb}} = 0.05 \text{ FWHM}$ and $\sigma(\text{EW})_{\text{orb}} = 0.10 \text{ EW}$. Three epochs (the 2022 INT campaign on V404 Cyg, the 1995 WHT on GS2000+25 and the 2013 GTC on Swift J1357.2-0933) have significantly larger variability in FWHM than the remaining 21, but this is caused by statistical noise because the individual spectra in these campaigns have very poor signal-to-noise ratios $S/N \leq 3$ compared to the rest, which typically have $S/N \geq 10$. In any case, excluding these three epochs does not change the linear fits. The effect of these three epochs on the EW variability (which is an integrated line flux) is otherwise negligible, despite the poor quality of the spectra. On the basis of Fig. A.2, and in the absence of a better approach, we decided to adopt orbital fractional errors that are constant for all the systems, i.e. $\sigma(\text{FWHM})_{\text{orb}}/\text{FWHM} = 0.05$ and $\sigma(\text{EW})_{\text{orb}}/\text{EW} = 0.10$.

Figure A.1 also depicts clear changes in the FWHM and EW mean values from epoch to epoch. These might be caused by geometric changes in a precessing accretion disc (see Zurita et al. 2002a, Torres et al. 2004, Calvelo et al. 2009, Zurita et al. 2016), although stronger support is needed for confirmation. Alternative explanations, such as fluctuations in the mass accretion rate, may also be responsible. For example, Cantrell et al. (2008) has shown that quiescent BH XRTs can sometimes transition between different optical states with distinct associated levels of aperiodic variability. In addition, a long-term brightening of the optical continuum has been reported in several XRTs, possibly caused by matter accumulating in the disc between outbursts (see Russell et al. 2018 and included references).

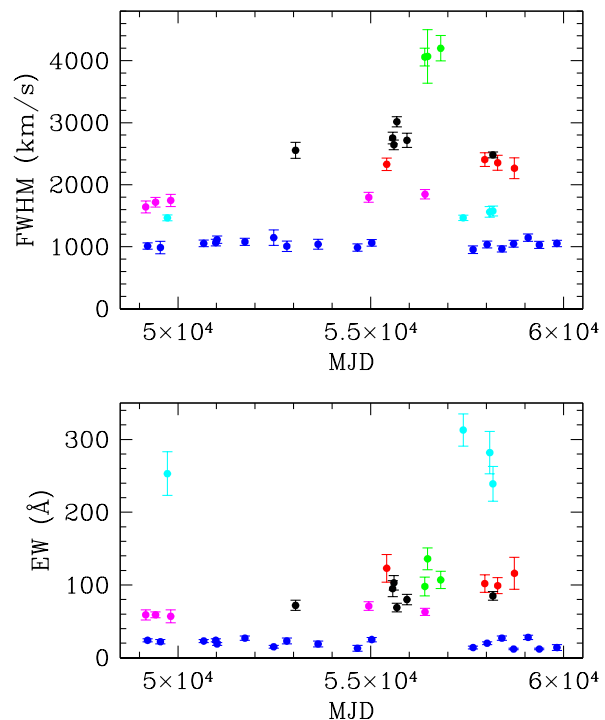


Fig. A.3. Long-term (secular) variation of FWHM and EW in a sample of quiescent BH XRTs. The plot covers a period of 30 years. Every point represents an orbital average over a single epoch. The color code is as follows: blue (V404 Cyg), cyan (GRO J0422+32), magenta (N. Mus 91), red (XTE J1859+226), black (XTE J1118+480) and green (SWIFT J1357.2-0933).

To quantify the long-term variations in FWHM and EW we have calculated the standard deviation of orbitally averaged measurements in 9 BHs with $\geq 25\%$ phase coverage spanning at least 3 different epochs. Figure A.3, for example, shows the secular FWHM and EW variability of a sample of BH XRTs through different epochs. The small sample size does not allow a detailed analysis, although the plot suggests that there is a stable mean value for each system with superimposed secular variability. The amplitude of the variability also appears to increase with the mean, so we again assume that a constant fractional variability can be adopted for all the systems. The average fractional standard deviation of the 9 BHs is $\sigma(\text{FWHM})_{\text{sec}} = 0.04 \text{ FWHM}$ and $\sigma(\text{EW})_{\text{sec}} = 0.13 \text{ EW}$. We consider these as a new source of systematic error that need to be added quadratically to FWHM and EW measurements obtained from single-epoch data (e.g. N. Vel 93).

The FWHM and EW values given for each epoch in Table A.1 do include the above systematic orbital and secular uncertainties, where necessary. With these new added systematic uncertainties, we have calculated the mean and standard deviation in the distribution of individual FWHM and EW values for each of the 20 BH XRTs. These are the final numbers listed in Table 1 and used in the main body of the paper.

Table A.1. Multi-epoch FWHM and EW of H α lines in quiescent BH XRTs

Object	Telescope	Year	Day	MJD	# spectra	Orbital Coverage	FWHM (km s ⁻¹)	EW (Å)	References
V404 Cyg	WHT	1993	12 Aug	49212.58	6	5 %	1011±52	24±2	1
	WHT	1994	6 & 13-14 July	49544.50	21	20 %	988±101	22±3	2
	WHT	1997	6-7 Aug	50668.16	4	10 %	1054±53	23±2	2
	Keck	1998	17 June	50982.50	1 ^a	5 %	1067±53	24±2	3
	WHT	1998	6 & 19-20 July	51014.90	40	10 %	1114±59	19±2	3
	WHT	2000	10 July	51736.73	2	5 %	1080±56	27±3	3
	INT	2002	7 July	52483.69	2	5 %	1147±123	15±2	3
	INT/WHT	2003	1-5 & 8 July	52824.80	19	35 %	1009±84	23±4	3
	WHT	2005	16-22 Sept	53634.25	23	35 %	1040±80	19±4	3
	SPM 2.1 m	2008	5-8 July	54654.74	6	15 %	987±58	13±4	3
	Keck	2009	13 July	55025.98	14	5 %	1063±53	25±3	4
<i>After 2015 outburst</i>									
V404 Cyg	NOT	2016	21 Sept	57653.39	2	5 %	954±61	14±2	5
	NOT	2017	20 Sept	58017.58	2	5 %	1036±56	20±2	5
	NOT	2018	8 Aug & 7 Nov	58400.71	4	5 %	966±49	27±3	5
	NOT	2019	10 June & 18 Oct	58704.16	4	10 %	1049±55	12±1	6
	NOT	2020	18 Aug	59080.44	2	5 %	1146±59	28±3	6
	NOT	2021	21 June	59370.68	2	5 %	1030±58	12±1	6
	INT	2022	12-18 Aug, 3,5,13-14 Sept & 11 Nov	59827.31	92	70 %	1013±132	13±4	6
BW Cir	VLT	1995	3-4 Apr & 3-4 June	49864.19	18	30 %	1096±84	53±7	3
	VLT	1996	24-25 March & 22-23 May	50169.11	14	35 %	1083±85	54±10	3
<i>After 1997 outburst</i>									
BW Cir	VLT	2000	22-23 Aug	51780.16	2	10 %	979±53	53±5	7
	VLT	2003	22-23 June	52814.46	13	15 %	1204±37	47±3	7
	VLT	2004	14-15 & 25-27 Apr	53142.76	42	40 %	990±37	60±3	7
	VLT	2006	27 Feb, 9,18 & 20-22 March	53814.40	11	25 %	1053±84	52±10	8
GX 339-4	VLT	2016	22 May, 9-10, 12, 14, 30-31 Aug & 3-7 Sept	57631.90	16 ^b	45 %	855±52	76±14	9
XTE J1550-564	VLT	2001	24-27 May	52053.78	18	30 %	1491±99	29±4	10
<i>After 2003 outburst</i>									
XTE J1550-564	Magellan Clay	2008	28 June & 3-4 Aug	54645.56	16	30 %	1419±139	29±6	11
MAXI J1820+070	GTC	2023	18-19, 23 July & 15, 17 Aug	60153.97	11	60 %	1678±85	75±19	6
N. Oph 77	Victor M. Blanco	1993	23 May	49131.09	1 ^a	65 %	1758±88	80±8	12
	Victor M. Blanco	1994	4-6 July	49539.87	1 ^b	65 %	2053±109	46±5	12
	Keck	1996	12 May	50215.98	1 ^b	20 %	1764±91	79±8	13
	Keck	1996	14 July	50278.87	1 ^b	50 %	2001±107	22±2	13
N. Mus 91	AAT	1993	25 June	49164.89	2	10 %	1642±96	59±7	14
	NTT	1994	5-7 March	49419.13	13	90 %	1718±77	59±4	14
	NTT	1995	3-4 April	49812.21	16	95 %	1747±98	57±9	14
	Magellan Clay	2009	25 April	54947.47	40	90 %	1796±80	71±6	15
	VLT	2013	12-14, 28 April & 9 May	56407.04	17	80 %	1847±76	63±5	16
MAXI J1305-704	VLT	2016	31 March	57479.70	16	95 %	2350±203	33±6 ^c	17
GS 2000+25	Keck	1995	22 July	49920.81	1 ^a	100 %	2261±117	24±3	18
	WHT	1995	24-26 July	49925.29	1 ^a	100 %	2119±121	34±4	19
A 0620-00	WHT	1991-92	31 Dec-1 Jan	48621.67	1 ^b	90 %	1921±96	61±7 ^d	20
	VLT	2000	6, 16 & 20 Dec	51889.72	20	40 %	1939±69	44±12	21
	Magellan Clay	2006	14-16 Dec	54085.67	1 ^b	100 %	1855±93	74±7 ^d	22
	GTC	2012	5-6 Dec	56268.18	40	55 %	2043±51	50±5	23
	GTC	2013	7 Jan	56300.49	38	80 %	1894±70	69±5	23
	GTC	2018	17 Feb	58167.39	12	5 %	1776±92	61±7	24
XTE J1650-500	VLT	2002	10 June	52436.70	1 ^a	100 %	1898±121	9±2	25-26
N. Vel 93	Keck	1998-99	1 Feb, 5-6 Mar 98 & 22 Jan 99	52436.70	1 ^a	70 %	2055±124	63±10	27
N. Oph 93	GTC	2020	22 June	59023.53	1 ^a	30 %	2267±194	89±15	28
XTE J1859+226	GTC	2010	17 June & 13 Aug	55413.55	10	80 %	2329±100	123±19	29
	GTC	2017	22-23 July	57957.88	26	100 %	2405±111	102±12	30
	GTC	2018	20 June	58290.62	2	15 %	2353±120	99±11	24
	GTC	2019	22-29 & 30-31 Aug	58725.22	10	85 %	2265±169	116±22	6
KY TrA	VLT	2016	4 & 7 April	57484.06	6	30 %	2167±185	56±18	31
GRO J0422+32	WHT	1994-95	28 Dec 94, 1 & 22 Feb 95	49726.18	17	100 %	1465±46	253±30	32
	GTC	2016	9 Jan	57397.49	18	100 %	1466±44	313±22	23
	GTC	2017	28 Nov	58086.50	3	20 %	1562±86	282±29	6
	GTC	2018	17 Feb	58167.36	2	15 %	1577±81	239±24	24
XTE J1118+480	Keck	2004	14 Feb	53050.00	1 ^a	100 %	2555±128	72±7	33-34
<i>After 2005 outburst</i>									
XTE J1118+480	GTC	2011	6 Jan	55568.66	25	70 %	2753±93	95±11	35-36
	GTC	2011	7 Feb	55600.63	36	95 %	2643±79	103±10	35-36
	GTC	2011	24 Apr	55676.53	36	100 %	3015±83	69±6	35-36
	GTC	2012	11 Jan	55938.68	34	95 %	2716±113	80±7	36-37
	GTC	2018	17 Feb	58167.47	9	35 %	2480±48	85±6	24
Swift J1753.5-0127	GTC	2018	12 July	58312.50	14	95 %	3592±175	166±14	38
	GTC	2018	13 July	58313.49	14	100 %	3435±140	159±23	38
	GTC	2018	14 July	58314.49	12	100 %	3499±114	171±13	38
Swift J1357.2-0933	VLT	2013	13, 17 Apr & 3 May	56402.02	24	90 %	4058±144	98±13	39
	GTC	2013	29-30 June	56473.99	4	80 %	4068±433	136±15	3
	GTC	2014	29-30 Apr, 2-3 & 28 June	56813.81	42	100 %	4200±205	107±12	40

Notes. ^(a) Values derived from a single or phase-averaged spectrum. ^(b) Values derived from a digitised phase-averaged spectrum. ^(c) Following (17) we have corrected the EW by a 27 per cent contribution of the interloper to the continuum. ^(d) EW values have been digitised from a figure of the corresponding paper.

Table A.1. continued.

Object	Telescope	Year	Day	MJD	spectra (#)	Orbital Coverage	FWHM (km s^{-1})	EW (\AA)	References
MAXI J1659-152	VLT	2013	6 June	56449.79	1 ^a	30 %	3309±361	130±23	41

References. (1) Casares & Charles (1994); (2) Casares (1996); (3) Casares (2015); (4) González Hernández et al. (2011); (5) Casares et al. (2019); (6) this paper; (7) Casares et al. (2004); (8) Casares et al. (2009); (9) Heida et al. (2017); (10) Orosz et al. (2002); (11) Orosz et al. (2011); (12) Remillard et al. (1996); (13) Filippenko et al. (1997); (14) Casares et al. (1997); (15) Wu et al. (2015); (16) González Hernández et al. (2017); (17) Mata Sánchez et al. (2021); (18) Casares et al. (1995a); (19) Filippenko et al. (1995); (20) Marsh et al. (1994); (21) González Hernández & Casares (2010); (22) Neilsen et al. (2008); (23) Casares et al. (2022); (24) Casares & Torres (2018); (25) Sánchez-Fernández et al. (2002); (26) Orosz et al. (2004); (27) Filippenko et al. (1999); (28) Casares et al. (2023); (29) Corral-Santana et al. (2011); (30) Yanes-Rizo et al. (2022); (31) Yanes-Rizo et al. (2024); (32) Casares et al. (1995b); (33) González Hernández et al. (2006); (34) González Hernández et al. (2008b); (35) González Hernández et al. (2012); (36) Zurita et al. (2016); (37) González Hernández et al. (2014); (38) Yanes-Rizo et al. (2025); (39) Torres et al. (2015); (40) Mata Sánchez et al. (2015); (41) Torres et al. (2021)

Table A.2. Quiescent epochs and magnitudes

Source	Outburst (Year)	Quiescence (MJD)	Quiescent Mags	References for Mags
V404 Cyg	1989	48814-57190	$V=18.42\pm0.02$, $R=16.52\pm0.01$	(1)
	2015	57405-	$V=18.2\pm0.3$	(2)
BW Cir	1987	~47200-50754	$R\sim20.2$, $I\sim19.2$	(3)
	1997	~51135-57000	$R\sim20-21$, $i'\sim19.7-20.8$	(3), (4)
GX 339-4 ^a	2014-5	57579-57990	$V\sim20$, $R\sim19$, $i\sim18.7$	(5)
XTE J1550-564	2001	52020-52719	$V\sim22$	(6)
	2003	52764-	$V\sim21.9$	(7)
MAXI J1820+070	2018	60106-	$g^s=19.31\pm0.02$, $r^s=18.58\pm0.01$, $i^s=18.22\pm0.01$	(8)
N. Oph 77	1977	48719-	$V=21.5\pm0.1$	(9)
N. Mus 91	1991	48736-	$V=20.66\pm0.03$, $R=19.75\pm0.27$, $I=19.00\pm0.22$	(10)
MAXI J1305-704	2012	56771-	$r^s=21.69\pm0.17$	(11)
GS 2000+25	1988	47763-	$R=21.21\pm0.15$	(12)
A 0620-00	1975	43053-	$V=18.25$, $R=17.00$	(13)
XTE J1650-500 ^b	2001	~52490-	$V\sim24$, $R\sim22$	(14)
N. Vel 93	1993	49846-	$R=20.6\pm0.1$	(15)
N. Oph 93	2016	58208-	$i^s=21.39\pm0.15$	(16)
XTE J1859+226	1999	51781-59250	$V=23.39\pm0.09$, $R=22.48\pm0.07$	(17)
KY TrA ^c	1990	48290-	$V=23.6\pm0.1$, $R=22.3\pm0.1$, $I=21.47\pm0.09$	(18)
GRO J0422+32	1992	49600-	$R=20.94\pm0.11$	(19)
XTE J1118+480	2000	52311-53375	$R=18.93\pm0.01$	(20)
	2005	53447-	$R\sim19$	(21)
Swift J1753.5-0127	2005	57907-60216	$V=22.17\pm0.25$, $I^s=21.00\pm0.14$	(22)
Swift J1357.2-0933	2011	56042-57845	$g^s=22.26\pm0.38$, $r^s=21.54\pm0.35$, $i^s=21.21\pm0.36$; $I\sim20-21$	(23), (24)
MAXI J1659-152	2010	56087-	$r^s=24.20\pm0.08$, $I=23.3\pm0.1$	(25)

References. (1) Casares et al. (1993); (2) Casares et al. (2022); (3) Casares et al. (2009); (4) Koljonen et al. (2016); (5) Russell et al. (2017); (6) Orosz et al. (2002); (7) Orosz et al. (2011); (8) Baglio et al. (2023); (9) Remillard et al. (1996); (10) King et al. (1996); (11) Mata Sánchez et al. (2021); (12) Callanan & Charles (1991); (13) Ciatti & Vittone (1977); (14) Garcia & Wilkes (2002); (15) Shahbaz et al. (1996); (16) Saikia et al. (2022); (17) Zurita et al. (2002b); (18) Zurita et al. (2015); (19) Garcia et al. (1996); (20) Zurita et al. (2002c); (21) Zurita et al. (2006); (22) Zhang et al. (2017); (23) Shahbaz et al. (2013); (24) Russell et al. (2018); (25) Corral-Santana et al. (2018).

Notes.

^(a) It shows outbursts every ~ 2.5 years. The following outburst took place in 2017. ^(b) The quiescent R-band magnitude quoted by Garcia & Wilkes (2002) is consistent with our own PSF analysis of a DECaPS image taken on 29 April 2017, which yields $r^s=22.10\pm0.12$. ^(c) The optical counterpart of KY TrA was lost after the $V>21$ upper limit reported by Murdin et al. (1977) during the decay of the 1974 discovery outburst. The quiescent counterpart was only recovered by Zurita et al. (2015) 17 years after a new mini-outburst was serendipitously discovered in 1990.

Appendix B: Empirical $P_{\text{orb}} - T_{\text{eff}}$ relation for low-mass donors in BH X-ray transients

In order to derive an empirical $P_{\text{orb}} - T_{\text{eff}}$ relation for donor stars in BH XRTs we start by collecting spectral types from the literature. The compilation is divided into two categories: low-mass companions $M_2 \lesssim 1.5 M_{\odot}$ and intermediate-mass companions $M_2 \approx 2 - 5 M_{\odot}$. The motivation for doing so is two-fold. On the one hand, XRTs with intermediate-mass companions (IMXBs) are thought to be precursors of those with low-mass companions (LMXBs), and thus represent a different evolutionary phase (Podsiadlowski et al. 2003). On the other, high luminosity donors in IMXBs totally veil disc emission lines, such as $H\alpha$, and, hence, are of little interest in the context of this paper. We therefore focus here on the group of BH LMXBs (Table B.1), although information on BH IMXBs is also provided for completeness (Table B.2). The categorisation of BW Cir is somewhat controversial because its donor is an early G-type star with a mass of $\approx 1 - 2.4 M_{\odot}$ that sits within the Hertzsprung gap (Casares et al. 2004). However, because of its moderately strong $H\alpha$ line, we tentatively consider BW Cir as a BH LMXB in this work.

Reported spectral types have been determined following three different methods: (1) a qualitative classification, based on the presence (or lack thereof) of distinct spectral features (e.g. the G -band at $\sim 4310 \text{ \AA}$, the Mg Ib triplet at $\sim 5170 \text{ \AA}$, TiO or CO molecular bands, etc.), either in the visible (VIS SPEC) or near-infrared (NIR SPEC) part of the spectrum. In some cases, the classification is more quantitative as it relies on figures of merit such as the intensity of the highest cross-correlation peak or a χ^2 minimisation of residuals after template subtraction. (2) Model fits to the observed (donor's dominated) multi-wavelength spectral energy distribution (SED). (3) a direct T_{eff} determination derived by fitting libraries of synthetic stellar models (SPEC FIT).

In the case of VIS/NIR SPEC and SED methods we transformed spectral types into T_{eff} values. To do so we assume that LMXB donors below the *bifurcation period* ($P_{\text{orb}} \lesssim 18 \text{ h}$; see Podsiadlowski et al. 2002) can be approximated by main sequence (MS) stars and, thus, adopt the T_{eff} scale from the empirical collection of table 5 in Pecaut & Mamajek (2013). For long period LMXBs ($P_{\text{orb}} \gtrsim 3 \text{ d}$) we follow instead the T_{eff} scale of giant stars from van Belle et al. (1999). Finally, LMXB donors with $18 \text{ h} \lesssim P_{\text{orb}} \lesssim 3 \text{ d}$ are considered subgiants, and their T_{eff} values interpolated between the MS and giant scales of Pecaut & Mamajek (2013) and van Belle et al. (1999).

To verify the reliability of these assumptions we have compared average densities $\langle \rho \rangle$ of LMXB companions with those of MS and giants stars of similar spectral types. The density of a Roche-lobe filling star is obtained by bringing the Roche lobe geometry into Kepler's third law. Adopting Paczyński's approximation for the volume-averaged Roche-lobe radius (Paczynski 1971) allows cancelling out the dependence on binary mass ratio q , leading to $\langle \rho \rangle \approx 110 \times P_{\text{orb}}^{-2}$, where P_{orb} is given in units of hours and $\langle \rho \rangle$ in gr cm^{-3} (Frank et al. 2002). If instead we use Eggleton's more accurate approximation (Eggleton 1983), we find

$$\langle \rho \rangle = 92.6 \times \frac{[0.6 q^{2/3} + \ln(1 + q^{1/3})]^3}{q(1 + q)} \times P_{\text{orb}}^{-2}, \quad (\text{B.1})$$

equation that weakly depends on q . We note the former expression $\langle \rho \rangle \approx 110 \times P_{\text{orb}}^{-2}$ is recovered for $q = 0.22$, which seems appropriate for cataclysmic variables. BH LMXBs, on the

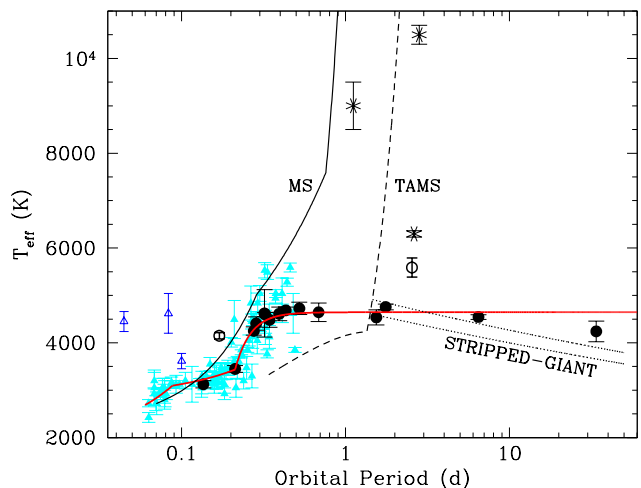


Fig. B.1. Observed T_{eff} vs orbital period (P_{orb}) for donor stars in BH XRTs. Asterisks indicate $\approx 2 - 5 M_{\odot}$ donor stars (IMXBs) while solid black circles low-mass $\lesssim 1.5 M_{\odot}$ donors (LMXBs). The open circles mark the position of the early G-type donor in BW Cir and the nuclear-evolved companion in XTE J1118+480. Solid triangles in cyan indicate donor stars in CVs from the compilation of Knigge (2006). The blue open triangles indicate the three nuclear-evolved donors in EI Psc, QZ Ser and SDSS 1702+3229. The red line shows our empirical fit to the group of CVs and BH LMXBs, excluding BW Cir and the nuclear-evolved companions in XTE J1118+480 and the three CVs. For comparison, we also plot T_{eff} tracks of main sequence (MS), terminal age main sequence (TAMS) and stripped-giant stars that would fill the Roche lobes for a given P_{orb} .

other hand, have more extreme mass ratios, with typical values $q \approx 0.06$ (cf Casares 2016), leading to $\langle \rho \rangle \approx 186 \times P_{\text{orb}}^{-2}$. Table B.3 presents an up-to-date collection of mass ratios in BH LMXBs and implied donor densities, according to eq. B.1. In any case, it should be noted that the use of Paczyński's approximation is equally valid as it leads to tiny differences in density on the order of $\approx 2-4 \%$. A direct comparison with MS and giant star densities supports our choice of T_{eff} scales for LMXB donors i.e. average donor densities above $P_{\text{orb}} \gtrsim 3 \text{ d}$ are in the range of giant stars while those with $P_{\text{orb}} \lesssim 18 \text{ h}$ are consistent with typical MS or slightly evolved (i.e. oversized) stars.

Tables B.1 and B.2 summarise the spectral types collected from the literature and their associated T_{eff} numbers. When several T_{eff} values are present for a given system, the average (marked in bold) is selected. This was computed as the unweighted mean after randomising the individual (independent) measurements. Here we have assumed flat probability distributions for all methods except SPEC FIT, where a normal distribution is adopted. The evolution of T_{eff} with P_{orb} is presented in Fig. B.1. For reference, we also plot $P_{\text{orb}} - T_{\text{eff}}$ tracks for MS and terminal age main sequence (TAMS) stars that would fit in their corresponding Roche lobes. To do so, we used eq. B.1 with $q = 0.06$ and mass-radius and mass- T_{eff} relations for MS (Pecaut & Mamajek 2013) and TAMS (Bertelli et al. 2008, 2009). In addition, we depict stripped-giant models to track the location of low-mass donors that have evolved off the MS. The radius and luminosity (and thus T_{eff}) of stripped-giant stars are uniquely determined by the mass of the degenerate helium core m_c , which is constrained between the total stellar mass M_2 and the Schönberg-Chandrasekhar limit $\sim 0.17 M_2$ (Webbink et al. 1983; King 1993). Both models, $m_c = 0.17 M_2$ (lower line) and $m_c = M_2$ (upper line), are displayed.

Table B.1. Spectral types and T_{eff} of donor stars in BH LMXBs

Object	P_{orb} (d)	Spect. Type	Method	T_{eff} (°K)	References for Spect. Type
GRS 1915+105	33.85(16)	K1-5 III	NIR SPEC	4241±219	1
V404 Cyg	6.471170(2)	G9-K1 III	VIS SPEC	4570±110	2
		G8-K2 III	SED	4570±219	3
		K2-4 III	NIR SPEC	4242±110	4
		–	SPEC FIT	4800±100	5
		–	–	4544±48	–
BW Cir	2.54451(8)	G0-5 IV	VIS SPEC	5589±201	6
GX 339-4	1.7587(5)	K1-2 IV	NIR SPEC	4756±60	7
XTE J1550-564	1.5420333(24)	K2-4 IV	VIS SPEC	4536±160	8
MAXI J1820+070	0.68549(1)	K3-5 V	VIS SPEC	4645±195	9
N. Oph 77	0.5228(44)	K1-5 V	VIS SPEC	4810±360	10
		K3-5 V ^a	VIS SPEC	4645±195	11
		–	–	4725±130	–
N. Mus 91	0.43260249(9)	K0-4 V	VIS SPEC	4950±330	12
		K3-5 V	VIS SPEC	4645±195	13
		K3-4 V	VIS SPEC	4730±110	14
		K4-6 V	VIS SPEC	4410±210	15
		–	–	4685±70	–
MAXI J1305-704	0.394(4)	–	SPEC FIT	4610±145	16
GS 2000+25	0.3440915(9)	K3-7 V	VIS SPEC	4445±395	17
		K3-6 V	VIS SPEC	4520±320	18
		–	–	4485±158	–
A 0620-00	0.32301415(7)	K5-7 V	VIS SPEC	4250±200	19
		K4-5 V	VIS SPEC	4535±85	20
		K3-7 V	VIS SPEC	4445±395	21
		K3-4 V	VIS SPEC	4730±110	22
		K0-5 V	NIR SPEC	4865±415	23
		K3-5 V ^b	SED	4600±200	24
		–	SPEC FIT	4900±100	25
		K5-7 V	NIR SPEC	4250±200	26
		K4-6 V ^c	NIR SPEC	4410±210	27
		–	SPEC FIT	5000±100	28
		–	–	4598±45	–
XTE J1650-500	0.3205(7)	K1-7 V ^d	VIS SPEC	4620±500	29
N. Vel 93	0.285206(1)	K0-5 V	VIS SPEC	486±415	30
		K7-M0 V	VIS SPEC	3950±100	31
		–	–	4407±142	–
XTE J1859+226	0.276(3)	K5-7 V	VIS SPEC	4250±200	32
		K5-7 V	VIS SPEC	4250±200	33
		–	–	4250±88	–
GRO J0422+32	0.2121600(2)	M0-5 V	VIS SPEC	3450±400	34
		M0-4 V	VIS SPEC	3520±325	35
		M1-4 V	VIS SPEC	3440±240	36
		M4-5 V	VIS SPEC	3125±75	37
		M0-2 V	SED	3700±150	38
		–	–	3448±70	–
XTE J1118+480	0.16993404(5)	K7-M0 V	VIS SPEC	3950±100	39
		K5-M1 V	VIS SPEC	4065±385	40
		K5-9 V ^e	SED	4165±285	41
		–	SPEC FIT	4700±100	42
		K7-M1 V	NIR SPEC	3865±185	43
		–	–	4148±66	–
SWIFT J1753.5-0127	0.1358(8)	M4-5 V	VIS SPEC	3125±75	44

References. (1) Harlaftis & Greiner (2004); (2) Casares & Charles (1994); (3) Hynes et al. (2009); (4) Khargharia et al. (2010); (5) González Hernández et al. (2011); (6) Casares et al. (2004); (7) Heida et al. (2017); (8) Orosz et al. (2011); (9) Torres et al. (2019); (10) Remillard et al. (1996); (11) Harlaftis et al. (1997); (12) Remillard et al. (1992); (13) Orosz et al. (1996); (14) Casares et al. (1997); (15) Wu et al. (2015); (16) Mata Sánchez et al. (2021); (17) Casares et al. (1995a); (18) Harlaftis et al. (1996); (19) Oke (1977); (20) Murdin et al. (1980); (21) McClintock & Remillard (1986); (22) Marsh et al. (1994); (23) Shahbaz et al. (1999a); (24) Gelino et al. (2001); (25) González Hernández et al. (2004); (26) Froning et al. (2007); (27) Harrison et al. (2007); (28) Zheng et al. (2022); (29) Orosz et al. (2004); (30) Shahbaz et al. (1996); (31) Filippenko et al. (1999); (32) Corral-Santana et al. (2011); (33) Yanes-Rizo et al. (2022); (34) Orosz & Bailyn (1995); (35) Casares et al. (1995b); (36) Harlaftis et al. (1999); (37) Webb et al. (2000); (38) Gelino & Harrison (2003); (39) Wagner et al. (2001); (40) McClintock et al. (2001); (41) Gelino et al. (2006); (42) González Hernández et al. (2008b); (43) Khargharia et al. (2013); (44) Yanes-Rizo et al. (2025).

Notes.

^(a) Although (11) report K3-M0, the clear lack of TiO bands in their spectra strongly suggests $\leq K5$. ^(b) We adopt an uncertainty of ± 1 sub-types on the spectral classification favoured by (24). ^(c) We adopt an uncertainty of ± 1 sub-types on the spectral classification favoured by (26). ^(d) The spectral type is poorly constrained by (28) because of limited quality spectra and thus we adopt a conservative uncertainty of ± 3 sub-types. ^(e) Following (26) we adopt an uncertainty of ± 2 sub-types on the favoured spectral classification.

Table B.2. Spectral types and T_{eff} of donor stars in BH IMXBs

Object	P_{orb} (d)	Spect. Type	Method	T_{eff} (°K)	References for Spect. Type
SAX J1819.3-2525	2.81730(1)	B9 III	SPEC FIT	10500±200	44
GRO J1655-40	2.621928(4)	F3-6 IV	VIS SPEC	6395±177	45
		F5-7 IV	VIS SPEC	6236±122	46
		–	SPEC FIT	6400±250	47
		–	SPEC FIT	6500±50	48
		F5-G0 IV	SED	6150±350	49
		–	SPEC FIT	6100±200	50
		–	–	6297±68	–
4U 1543-475	1.116407(3)	A2±1 V	SPEC FIT	9000±500	51

References. (44) Orosz et al. (2001); (45) Orosz & Bailyn (1997); (46) Shahbaz et al. (1999b); (47) Israelian et al. (1999); (48) Buxton & Vennes (2001); (49) Beer & Podsiadlowski (2002); (50) González Hernández et al. (2008a); (51) Orosz et al. (1998).

Table B.3. Donor star densities in BH LMXBs (marked in bold), compared to those of MS and Giants with same spectral type.

Object	P_{orb} (d)	q	$\langle\rho\rangle$ (gr cm ⁻³)	Spec Type ^a	$\langle\rho_{\text{MS}}\rangle^b$ (gr cm ⁻³)	$\langle\rho_{\text{GIANT}}\rangle^c$ (gr cm ⁻³)	References for q
GRS 1915+105	33.85	0.042(24)	2×10^{-4}	K1-5	2.4-2.9	$1-4\times 10^{-4}$	(1)
V404 Cyg	6.471	0.067(5)	5×10^{-3}	G8-K4	1.7-2.8	$1-9\times 10^{-4}$	(2)
BW Cir	2.544	0.12(3)	0.03	G0-5	1.1-1.5	$1-6\times 10^{-3}$	(3)
GX 339-4	1.759	0.18(5)	0.06	K1-2	2.4	$3-4\times 10^{-4}$	(4)
XTE J1550-564	1.542	0.033(8)	0.08	K2-4	2.4-2.8	$1-3\times 10^{-4}$	(5)
MAXI J1820+070	0.685	0.072(12)	0.41	K3-5	2.6-2.9	$1-2\times 10^{-4}$	(6)
N Oph 77	0.523	0.014(16)	0.65	K1-5	2.4-2.9	$1-4\times 10^{-4}$	(7)
N Mus 91	0.433	0.079(7)	1.03	K0-6	2.3-3.3	$1-4\times 10^{-4}$	(8)
MAXI J1305-704	0.394	0.05(2)	1.22	K3-5	2.6-2.9	$1-2\times 10^{-4}$	(9)
GS 2000+25	0.344	0.042(12)	1.58	K3-7	2.6-3.6	$0.7-2\times 10^{-4}$	(10)
A 0620-00	0.323	0.067(10)	1.83	K0-7	2.3-3.6	$0.7-4\times 10^{-4}$	(11)
XTE J1650-500	0.321	0.03(3)	1.80	K1-7	2.4-3.6	$0.7-4\times 10^{-4}$	(12)
N Vel 93	0.285	0.055(10)	2.33	K0-M0	2.3-4.0	$0.3-4\times 10^{-4}$	(13)
XTE J1859+226	0.276	0.07(1)	2.52	K5-7	2.9-3.6	$0.7-1\times 10^{-4}$	(14)
GRO J0422+32	0.212	0.12(8)	4.35	M0-5	4.0-30	$\lesssim 3\times 10^{-5}$	(15)
XTE J1118+480	0.170	0.024(9)	6.32	K5-M1	2.9-5.6	$0.3-1\times 10^{-4}$	(16)
SWIFT J1753.5-0127	0.136	0.027(3)	9.96	M4-5	16-30	$\lesssim 3\times 10^{-5}$	(17)

Notes.

^(a) Widest spectral range given by Table B.1. ^(b) MS densities derived from the compilation of masses and radii of Pecaut & Mamajek (2013).

^(c) Giant densities from Drilling & Landolt (2002).

References. (1) Steeghs et al. (2013); (2) Casares (1996); (3) Casares et al. (2009); (4) Heida et al. (2017); (5) Orosz et al. (2011); (6) Torres et al. (2020); (7) Harlaftis et al. (1997); (8) Wu et al. (2015); (9) Mata Sánchez et al. (2021); (10) Harlaftis et al. (1996); (11) Marsh et al. (1994); (12) Casares (1996); (13) Macias et al. (2011); (14) Yanes-Rizo et al. (2022); (15) Harlaftis et al. (1999); (16) González Hernández et al. (2014); (17) Yanes-Rizo et al. (2025).

Figure B.1 shows that LMXB donors with $P_{\text{orb}} \gtrsim 1.5$ d have crossed the TAMS line and follow the stripped-giant branch, while those with $P_{\text{orb}} \lesssim 1.5$ d have not left the MS. In particular, donors with $P_{\text{orb}} \lesssim 0.3$ d (≈ 7 h) are only slightly evolved compared to MS stars on the empirical track of Pecaut & Mamajek (2013). XTE J1118+480 is a clear outlier since it is ~ 500 K hotter than expected for a MS at its orbital period. This is reminiscent of the cataclysmic variables QZ Ser, EI Psc and SDSS J1702+3229, whose donors are thought to descend from more massive progenitors that were significantly evolved at the onset of mass transfer (Thorstensen et al. 2002a,b; Littlefair et al. 2006). Interestingly, XTE J1118+480 has shown evidence for CNO processed material, in support for a highly evolved donor progenitor (Haswell et al. 2002).

Overall, LMXB donors are seen to follow a well-defined path in the $P_{\text{orb}} - T_{\text{eff}}$ plane. Unfortunately, this is weakly constrained at short orbital periods $\lesssim 0.14$ d due to lack of data. To compensate for this we decided to include an updated collection of CV donor spectral types from Knigge (2006). These have been converted to T_{eff} values, as was previously done for BH LMXBs. The addition of CV information seems justified, since previous work has shown that, for the same orbital period, donor stars in CVs and LMXBs are almost indistinguishable (e.g. Smith & Dhillion 1998).

In order to characterise the T_{eff} evolution with P_{orb} we fit the ensemble of BH LMXB and CV data points in three different regions: (i) short-periods below the period gap $P_{\text{orb}} \leq 0.085$ d (ii) intermediate-periods $0.085 \text{ d} \leq P_{\text{orb}} \leq 0.2$ d and (iii) long-

periods $P_{\text{orb}} \geq 0.2$ d. We find that a broken power-law provides a good description of the long-period systems, while simple linear fits are used for shorter periods i.e.

$$T_{\text{eff}} = \begin{cases} 1810 + 14611 \times P_{\text{orb}} & P_{\text{orb}} < 0.085 \text{ d} \\ 2856 + 2732 \times P_{\text{orb}} & 0.085 \text{ d} \leq P_{\text{orb}} < 0.213 \text{ d} \\ 4645 - 1.09 \times P_{\text{orb}}^{-4.52} & 0.213 \text{ d} \leq P_{\text{orb}} \end{cases} \quad (\text{B.2})$$

These empirical fits are represented by the red line in Fig. B.1. For the reasons given above, the five outliers (BW Cir, XTE J1118+480 plus the three CVs with confirmed nuclear-evolved donors) were masked in the fits. We note, however, that their inclusion does not significantly alter the results of the fits.

The surprisingly narrow path traced by LMXB donors in the $P_{\text{orb}} - T_{\text{eff}}$ plane suggests that they all follow the same evolutionary track. King, Kolb & Burderi (1996) showed that systems with $P_{\text{orb}} \lesssim 2$ d evolve towards shorter periods because angular momentum losses shrink the binary orbit faster than stellar expansion. Conversely, for $P_{\text{orb}} \gtrsim 2$ d the companion is nuclear-evolved before the onset of mass transfer and the binary evolves to increasing orbital periods (see also Pylyser & Savonije 1988). The gap seen at $\approx 0.7 - 1.5$ d thus reflects a real shortage of systems triggered by the bifurcation period, which causes binaries to evolve towards either shorter or longer P_{orb} . In addition, the small scatter seen at periods ≈ 0.25 -1 d implies that the orbital separation after common envelope ejection must have been sufficiently tight for the donor stars to come into contact before evolving significantly. To obtain a better description of the $P_{\text{orb}} - T_{\text{eff}}$ relation for BH LMXBs at very short orbital periods ≤ 0.15 d, it would be important to determine spectral types for the donor stars in Swift J1357.2-0933 (0.12 d) and MAXI J1659-152 (0.10 d). This will require infrared spectroscopy since these stars are too cold to be detected at visible wavelengths (Mata Sánchez et al. 2015; Torres et al. 2015, 2021).

Appendix C: A simulation of $H\alpha$ EWs in quiescent BH X-ray transients

We have built a toy model to simulate the EW of the $H\alpha$ emission in quiescent BH XRTs. We assume typical BH XRT parameters, with a compact object mass $M_1 = 8 M_{\odot}$ and mass ratio $q = 0.06$. The binary separation is set by Kepler's Third law $a \propto (P_{\text{orb}}^2 M_1 (1+q))^{1/3}$ and the size of the secondary star by the effective Roche lobe radius through Eggleton's approximation $R_2/a = 0.49 q^{2/3} / [(0.6 q^{2/3} + \ln(1+q^{2/3}))]$ (Eggleton 1983). The accretion disc is simulated by a flat cylinder truncated at the 3:1 resonance radius $r_d/a = (1/3)^{2/3} (1+q)^{-1/3}$ (Frank et al. 2002). Based on observations of extreme wing velocities in $H\alpha$ profiles we set the inner disc radius at $r_{\text{in}} = 0.06 r_d$ (Casares et al. 2022), although this parameter has very little impact on the results of the simulation.

To estimate the EW of the $H\alpha$ line we start by computing the continuum emitted by the secondary star and the accretion disc using blackbody approximations. The flux density radiated by the secondary star, $f_s(\lambda)$, is obtained from a blackbody with radius R_2 and temperature T_{eff} , where T_{eff} depends on P_{orb} according to eq. B.2. For the flux density of the accretion disc continuum, $f_d(\lambda)$, we adopt a multi-colour blackbody with a flat temperature profile $T_r = T_{\text{in}}(r/r_{\text{in}})^{-0.25}$ and inner disc temperature $T_{\text{in}} = 4500$ K, which are appropriate choices for the quiescent state (Orosz & Bailyn 1997; Beer & Podsiadlowski 2002). In

order to reproduce the far ultraviolet excess widely observed in quiescent BH XRTs (McClintock et al. 1995, 2003; Froning et al. 2011; Hynes & Robinson 2012; Poutanen et al. 2022) we also include emission from a hot blackbody, $f_h(\lambda)$, with temperature $T_h = 10000$ K and size $r_h = r_{\text{in}}$. This component has been attributed to the transition region between the thin disc and an advection dominated flow, although an origin on the bright spot, where the gas stream hits the outer disc, cannot be excluded (see Froning et al. 2011; Hynes & Robinson 2012).

To simulate the $H\alpha$ flux we assume optically thin emission from the surface of the accretion disc. We approximate the $H\alpha$ profile by a Gaussian function with an integrated flux $F_{H\alpha}$ which is proportional to the area of the accretion disc $\pi(r_d^2 - r_{\text{in}}^2)$. $F_{H\alpha}$ has been scaled to give $\text{EW} = 58 \text{ \AA}$ for the binary parameters of the canonical BH XRT A0620-00. The EW of the $H\alpha$ line is then calculated as

$$\text{EW}(H\alpha) = \frac{F_{H\alpha}}{f_s(\lambda_0) + \cos i [f_d(\lambda_0) + f_h(\lambda_0)]} \quad (\text{C.1})$$

with $\lambda_0 = 6563 \text{ \AA}$. The $\cos i$ factor accounts for the foreshortening of the accretion disc flux caused by binary inclination. In this crude approximation we neglect limb darkening as it has little effect on our limited λ and T_{eff} range of interest. As an example, Fig. C.1 presents the simulated spectral energy distribution (SED) for the case of A0620-00, where we adopt $P_{\text{orb}} = 0.323$ d, $q = 0.06$, $M_1 = 7 M_{\odot}$, $i = 53^\circ$ and $d = 1.1$ kpc (Cantrell et al. 2010). For reference, we also overlay NUV, optical and NIR photometric datapoints from Froning et al. (2011), dereddened with $E(B - V) = 0.35$ and $R_V = 3.1$. Our toy model provides a reasonable representation of the observed SED, taking into account the overarching simplifications, uncertainties in system parameters (e.g. the Gaia DR2 parallax gives $d = 1.6 \pm 0.4$ kpc Gandhi et al. 2019), and intrinsic variability common to quiescent XRTs (Cantrell et al. 2008). In any case, we emphasise that the simulation is not intended to be an accurate representation of the full SED for a given system, but an attempt to explore the dependence of the $H\alpha$ EW on binary parameters in a statistical way.

Since M_1 and the distance to the object cancel out in eq. C.1 our synthetic EWs depend only on P_{orb} , q and inclination. This is illustrated in the top panel of Fig. C.2, which represents the evolution of the EW with P_{orb} for a typical BH XRT with $q = 0.06$ and three different inclinations: $i = 33^\circ$, 60° and 81° i.e. the median and $\pm 1\sigma$ of the isotropic distribution. The figure shows that the EW is mostly determined by changes in the companion's temperature with P_{orb} (see Fig. B.1). Only at short periods $P_{\text{orb}} \lesssim 0.2$ d the drop in companion temperature does cause the disc contribution to start dominating the continuum flux. This amplifies the effect of inclination in reducing the disc brightness and, therefore, enlarges the range of possible EW values.

For comparison, we also simulate the evolution of the EW for the case of CVs (bottom panel in Fig. C.2). CVs have less extreme mass ratios, with typical values ranging between $q \approx 0.1 - 1$ and a mean at $q \approx 0.6$ (Ritter & Kolb 2003). Since mass ratio is known to increase with P_{orb} we apply here the relation derived in C18, i.e. $q = 0.73 - 11.55 \times \exp[-(P_{\text{orb}} + 0.39)/0.15]$. We also include an additional blackbody to account for the white dwarf emission, with fiducial parameters $T_{\text{WD}} = 15000$ K and $r_{\text{WD}} = 0.01 R_{\odot}$ (Savourey et al. 2011). The figure shows that EWs are systematically lower in CVs than in BH XRTs, a natural consequence of their larger q values, which increase the relative contribution of the companion to the total flux. Only below the period gap $P_{\text{orb}} \leq 0.085$ d, CV mass ratios begin to compare to

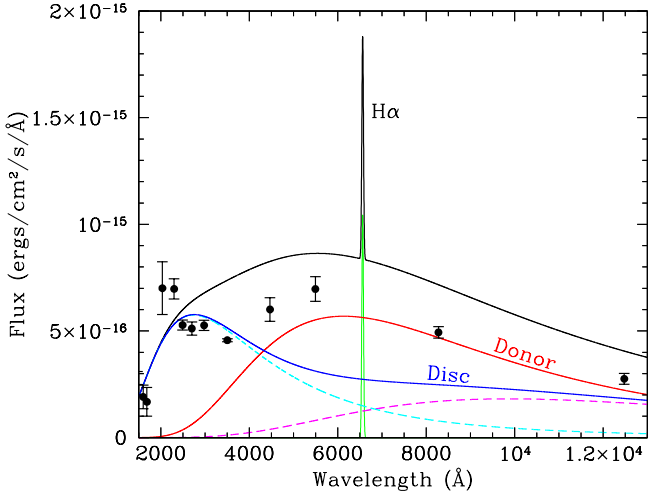


Fig. C.1. SED of A0620-00 simulated with our toy model, using the physical parameters of Cantrell et al. (2010). The accretion disc contribution to the SED (blue) consists of a multicolour blackbody (dashed magenta) plus an inner hot-spot with $T_h = 10000$ K (dashed cyan). The flux of the $H\alpha$ line (green Gaussian) has been scaled so that $EW=58$ Å. For comparison, we overlay SED photometric points from Froning et al. (2011).

those in BH XRTs, but then the contribution of the white dwarf continuum becomes important, capping the observed EWs. In summary, our simulation predicts that the combined effect of large mass ratios and dilution by the white dwarf continuum (most important at very short P_{orb}), leads to smaller EWs for CVs than for BH XRTs.

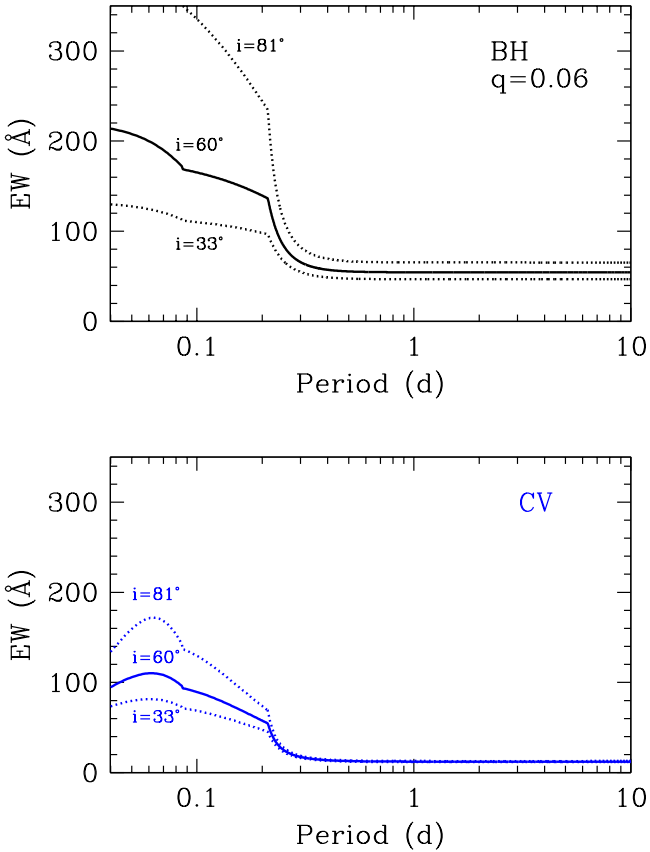


Fig. C.2. Simulated EWs as a function of orbital period for BH XRTs (top panel) and CVs (bottom panel). In the latter case we add the contribution of a white dwarf with $T_{\text{WD}} = 15000$ K and $r_{\text{WD}} = 0.01 R_{\odot}$ to the continuum. Also, the $P_{\text{orb}} - q$ dependence, derived in C18, is applied. Three different inclinations are represented.